Astronomy & Astrophysics manuscript no. N1377_B7_HR_astroph
July 16, 2020

ALMA resolves the remarkable molecular jet and rotating wind in the extremely radio-quiet galaxy NGC 1377

S. Aalto[1], N. Falstad[1], S. Muller[1], K. Wada[2], J. S. Gallagher[3], S. König[1], K. Sakamoto[4], W. Vlemmings[1], C. Ceccobello[1], K. Dasyra[5], F. Combes[6], S. García-Burillo[7], Y. Oya[10], S. Martín[8,9], P. van der Werf[11], A. S. Evans[12], and J. Kotilainen[13]

(Affiliations can be found after the references)

Received xx; accepted xx

ABSTRACT

Submillimetre and millimetre line and continuum observations are important in probing the morphology, column density, and dynamics of the molecular gas and dust around obscured active galactic nuclei (AGNs) and their mechanical feedback. With very high-resolution (0.″02 × 0.″03 (2 × 3 pc)) ALMA 345 GHz observations of CO 3–2, HCO^+ 4–3, vibrationally excited HCN 4–3 ν_2=1f, and continuum we have studied the remarkable, extremely radio-quiet, molecular jet and wind of the lenticular galaxy NGC 1377. The outflow structure is resolved, revealing a 150 pc long, clumpy, high-velocity (∼600 km s^{-1}), collimated molecular jet where the molecular emission is emerging from the spine of the jet with an average diameter of 3-7 pc. The jet widens to 10-15 pc about 25 pc from the centre, which is possibly due to jet-wind interactions. A narrow-angle (50°-70°), misaligned and rotating molecular wind surrounds the jet, and both are enveloped by a larger-scale CO-emitting structure at near-systemic velocity. The jet and narrow wind have steep radial gas excitation gradients and appear turbulent with high gas dispersion (σ>40 km s^{-1}). The jet shows velocity reversals that we propose are caused by precession, or more episodic directional changes. We discuss the mechanisms powering the outflow, and we find that an important process for the molecular jet and narrow wind is likely magneto-centrifugal driving. In contrast, the large-scale CO-envelope may be a slow wind, or cocoon that stems from jet-wind interactions. An asymmetric, nuclear r∼2 pc dust structure with a high inferred molecular column density $N(H_2) \simeq 1.8 \times 10^{24}$cm^{-2} is detected in continuum and also shows compact emission from vibrationally excited HCN. The nuclear dust emission is hot (T_d>180 K) and its luminosity is likely powered by a buried AGN. The lopsided structure appears to be a warped disk, which is responsible for a significant part of the nuclear obscuration and possibly formed as a result of uneven gas inflows. The dynamical mass inside r=1.4 pc is estimated to $9^{+2}_{-3} \times 10^6$ M$_\odot$, implying that the supermassive black hole (SMBH) has a high mass with respect to the stellar velocity dispersion of NGC 1377. We suggest that the SMBH of NGC 1377 is currently in a state of moderate growth, at the end of a more intense phase of accretion and also evolving from a state of more extreme nuclear obscuration. The nuclear growth may be fuelled by low-angular momentum gas inflowing from the gas ejected in the molecular jet and wind. Such a feedback-loop of cyclic outflows and central accretion could explain why there is still a significant reservoir of molecular gas in this ageing, lenticular galaxy. A feedback-loop would be an effective process in growing the nuclear SMBH and thus would constitute an important phase in the evolution of NGC 1377. This also invites new questions as to SMBH growth processes in obscured, dusty galaxies.

Key words. galaxies: evolution — galaxies: individual: NGC 1377 — galaxies: active — galaxies: nuclei — ISM: molecules — ISM: jets and outflows

1. Introduction

Feedback in the form of outflows and winds is an important process in regulating both the evolution of the stellar constituent of galaxies and the growth of their nuclear, supermassive black holes (SMBHs). Studying the link between accretion and the feedback of SMBHs (=active galactic nuclei, AGN) as well as star formation is essential for our understanding of how black holes and host galaxies evolve together (e.g. Ho 2004).

The most active growth phase is suspected to commence when the SMBH is deeply dust enshrouded (e.g. Lusso et al. 2013; Kocevski et al. 2015), but please see Ricci et al. (2017) for an additional discussion on the link between obscuration and accretion. Some of the nuclear obscuration is believed to occur in the form of a parsec-scale dusty torus which the Atacama Large Millimeter/submm Array (ALMA) is now able to image (e.g. García-Burillo et al. 2016; Gallimore et al. 2016; Aalto et al. 2017; Combes et al. 2019; Impellizzeri et al. 2019; García-Burillo et al. 2019). Feedback from the AGN eventually clears its surroundings and AGN outflows can eject large amounts of molecular gas from galaxy nuclei (e.g. Cicone et al. 2014; Fiore et al. 2017). In some cases the feedback impacts the evolution of the galaxy on time scales of only a few tens of Myr. The fate of the gas in the outflow is an important factor in determining whether the feedback turns off the growth of the galaxy for a long time, or whether the evolution is simply suspended. One question is if the gas in the outflow will leave the galaxy, or if it will return to support further growth (e.g. Aalto et al. 2012; Pereira-Santaella et al. 2018; Fluetsch et al. 2019).

The AGN feedback is presumed to turn off the nuclear growth, for example, by removing gas in the vicinity of the activity, but also through radiative feedback that heat the nuclear region preventing further growth. Recently there have been ideas that an outflow may also provide positive feedback in the form of star formation (Maiolino et al. 2017). Jets may also aid accretion through removing angular momentum from the gas in the inner region, allowing the remaining gas to reach the SMBH

(e.g. Blandford & Payne 1982; Aalto et al. 2016). Cold gas is an important fuel for SMBH accretion, since hot gas feeding is difficult, and it may occur via inflows along the disk in a bar or spiral arms, or through gas returning in a fountain, that is from gas decelerating in an outflow, stripped of its angular momentum. The importance of positive feedback for galaxy evolution is not well studied and requires further observational attention.

NGC 1377 is a nearby (21 Mpc (1″=102 pc)) lenticular galaxy with a far-infrared (FIR) luminosity of $L_{\rm FIR}$=4.3 × 10^9 $L_\odot$ (Roussel et al. 2003). It is extremely radio-quiet and significantly off the radio-FIR correlation (Helou et al. 1985); its radio emission is weaker (with respect to its FIR emission) by a factor ≈37 compared to normal galaxies (Roussel et al. 2003, 2006; Costagliola et al. 2016). The central region is dust-enshrouded (e.g. Spoon et al. 2007) and the source of the FIR luminosity (and the cause of its radio deficiency) has remained elusive. A nascent starburst (Roussel et al. 2003, 2006) or a radio-quiet AGN (Imanishi 2006; Imanishi et al. 2009) have been proposed as possible solutions. Costagliola et al. (2016) detect faint radio emission with a synchrotron spectrum and estimate a star formation rate (SFR) <0.1 $M_\odot$ yr^{-1} based on the radio emission. This is not sufficient to power the observed IR luminosity and supports the notion of a radio-quiet AGN. A powerful molecular outflow with a mass outflow rate of 8 – 35 $M_\odot$ yr^{-1} was found with the Submillimeter Array (SMA) (Aalto et al. 2012). ALMA observations revealed that the high-velocity gas is in the form of a collimated outflow - a molecular jet with a high momentum flux of >14 L/c. Velocity reversals along the molecular jet are suggested to be indications of precession (Aalto et al. 2016). ALMA also revealed a slow wind along the minor axis and the relation between the molecular jet and wind is not clear.

Although the high degree of collimation, combined with the large momentum flux, point towards an AGN, the nature of the power source behind the molecular outflow, and the FIR luminosity, is still not fully understood. Jets are indeed generally identified with accretion (Blandford 1998) consistent with an AGN. However, it is not clear if the molecular gas is carried out by an extremely faint radio-jet powered by inefficient, hot ("radio-mode") accretion, or if it is driven by effective accretion of cold gas ("quasar-mode"). In the latter case, the molecular jet would represent an unexplored form of quasar-mode feedback, where the high-velocity gas is expelled in a collimated outflow and not a wide-angle wind (Veilleux et al. 2013). It is also possible that the outflow may be powered by accretion onto the nuclear disk, and not onto the SMBH. This would then be a new form of outflow not previously seen in galactic-scale outflows.

Observations at mid-infrared (mid-IR) wavelengths reveal a compact (<0.″14), high surface brightness source (Imanishi et al. 2011) in the nucleus of NGC 1377 suggesting hot dust. This is consistent with the presence of nuclear vibrationally excited HCN emission which requires a 14 μm background temperature of $T_{\rm B}$(14 μm)>100 K to be excited (Aalto et al. 2015a, 2016). It is not clear whether this structure is part of an obscuring torus or disk, and whether it is opaque enough to absorb X-rays emerging from an accreting SMBH. It is also not understood whether (or how) the obscuring material is linked to the outflowing gas in the jet. High-resolution CO 6–5 observations (Aalto et al. 2017) reveal warm (T>100 K) nuclear gas at the base of the molecular outflow and also an apparent circumnuclear disk (CND) or torus of radius r=2.5 pc, but no nuclear submm continuum is detected.

In this paper we present new high resolution (0.″025 × 0.″033) (2.5 × 3 pc) ALMA CO J= 3–2, HCO^+ J=4–3, HCN J=4–3 ν_2=1f and also $H^{13}CN$ J=4–3 of NGC 1377. The paper is organised as follows: In Sec. 2 we present the observations and in Sec. 3 we show the results in the form of moment maps as well as images of the high-velocity, and low-velocity, CO 3–2 emission. We also present the 0.8 mm continuum image. In Sec. 4 we present the physical conditions (temperature and dispersion) of the gas and dust in nucleus and outflow components. In Sec. 5 we discuss the nuclear properties of NGC 1377 including the gas and dust column density, nuclear dynamics and enclosed mass, evidence for a gas inflow and a discussion of the luminosity source. We discuss the energetics and turbulence of the jet and wind in Sec. 6 and in Sec. 7 we discuss the origin and possible driving mechanisms of the jet and wind. In Sec. 8 we briefly discuss the larger scale disk rotation and mass. Finally we place the properties of the jet and wind of NGC 1377 in the context of its nuclear growth (Sec. 9).

2. Observations

Observations of the CO J=3–2 line (at 0.″25 × 0.″18 resolution) have been previously obtained with the Atacama Large Millimeter/submm Array (ALMA) in August 2014 and reported in Aalto et al. (2016). Here we present new ALMA observations, with the same spectral tuning but with more extended array configurations, taken in November 2017. A journal of the observations, including the 2014 lower resolution observations, is given in Table 1. The phase centre was set to R.A.=03h36m39.074, Dec.=−20d54m07.0553 (ICRS).

The correlator was set up with four 1.875 GHz-wide spectral windows centred at 342.2, 343.8 (covering the CO J=3–2 line, rest frequency 345.79599 GHz), 354.7 (covering the HCO^+ J=4–3 and HCN J=4–3 ν=1f, lines, rest frequencies 356.73422 and 356.25557 GHz, respectively), and 356.1 GHz, with a native channel spacing of ~2 MHz.

After calibration within the CASA reduction package, the visibility set was imported into the AIPS package for further imaging. The synthesised beam is 0.″030 × 0.″022 (3×2.2 pc for NGC 1377) with position angle PA=59°. With Briggs weighting (parameter robust set to 0.5), the resulting data has a sensitivity of 0.36 mJy per beam in a 10 km s^{-1} (12 MHz) channel width.

3. Results

3.1. CO emission features: Jet, wind, and disk

The CO emission delineates several apparently separate features:

- **a.** A well collimated structure which essentially is visible at high velocities. We interpret the high-velocity feature as a molecular jet (see Aalto et al. (2016)) and we refer to it as such throughout this paper.
- **b.** Minor axis emission at intermediate-to-low (30 to 80 km s^{-1}) velocities, a v-shaped structure which surrounds the high-velocity jet - in particular to the north of the nucleus and most prominent on the redshifted, eastern side. We refer to this structure as the narrow wind.
- **c.** Wide (width of ~2″)), minor-axis emission at low (20-30 km s^{-1}projected) velocities. The velocity shift between north and south is very small. We refer to this feature as the slow wind (or cocoon (Sec. 6.4)).
- **d.** There is also gas aligned with the stellar thick disk (on scales out to r=60-100 pc) and we refer to this as the disk, although, as we shall see, it is unclear if the gas is actually in a rotating disk.
- **e.** Gas in the inner r=5 pc is denominated the nucleus.

Table 1: Journal of the observations.

Date of observations	N_{ant} (b)	PWV (c) (mm)	t_{on} (d) (min)	B_{min} / B_{max} (e) (m / km)	Bandpass calibrator	Flux calibrator ((f) Jy)	Gain calibrator
12 Aug 2014 (a1)	33	∼0.5	30	31 / 1.1	J 0423−0120	J 0334−401 (0.46 ± 0.14)	J 0340−2119
12 Nov 2017 (a2)	45	∼0.6	50	113 / 13.9	J 0522−3627	J 0522−3627 (4.81 ± 0.23)	J 0340−2119
21 Nov 2017 (a2)	47	0.4–0.6	50	92 / 8.5	J 0522−3627	J 0522−3627 (4.70 ± 0.19)	J 0340−2119

(*a*1) ALMA project number 2012.1.00900.S; (*a*2) ALMA project number 2017.1.0659.S; (*b*) Number of 12 m-antennas in the array; (*c*) Amount of precipitable water vapour in the atmosphere; (*d*) On-source time; (*e*) Respectively minimum and maximum projected baseline; (*f*) Flux density at 350 GHz, as retrieved from the ALMA flux monitoring database.

f. There are curved structures along the minor axis, generally perpendicular to the outflow. These features may be bow shocks and we refer to them as such in the paper.

To help the reader navigate the complex structure of the molecular gas of NGC 1377, we present the various regions in a cartoon "finder-chart" in the right panel of Fig. 1. In Aalto et al. (2012) the systemic velocity was suggested to be v_{sys}=1740 km s^{-1} based on the shape of the CO 2–1 line. Here we find a v_{sys}=1730 km s^{-1} of the nuclear rotation (optical velocity definition, see Sec. 3.3) and we define high-velocity gas as $v > 80$ km s^{-1} (dominated by the jet structure and the nucleus). We note however, that the jet also contains lower velocity emission and that high-velocity gas is also found in the nucleus.

3.2. CO 3–2 moment maps

In the high resolution data we recover ∼60% of the emission in the previous, 0.″25 × 0.″18 resolution CO 3–2 map (Aalto et al. 2016). Most of the missing flux originates in extended, low-velocity emission associated with the slow wind (feature c in Fig. 1). For the compact and collimated structures, such as the jet and narrow wind, we recover all of the previous flux. In this paper we focus on the small-scale structure of the jet, wind and disk of NGC 1377 and therefore settle with presenting the high resolution results only, without merging with the older, lower resolution data set.

The CO 3–2 integrated intensity (moment 0) map and velocity field (moment 1) are presented in Fig 2 and the dispersion map (moment 2) in Fig. 3. We smoothed to two channel resolution, then for the moment 0 map we clipped at the 3σ level, and for the moment 1 and 2 maps we clipped at 4σ. The velocity centroids were determined through a flux-weighted first moment of the spectrum of each pixel, therefore assigning one velocity to a spectral structure. The dispersion (σ) was determined through a flux-weighted second moment of the spectrum of each pixel. This corresponds to the one dimensional velocity dispersion (i.e. the FWHM line width (ΔV) of the spectrum divided by 2.35 for a Gaussian line profile).

3.2.1. Integrated intensity map

Bright CO 3–2 emission is found in the inner 0.″3 (30 pc) with an elongation along the minor axis. Intense emission is also located 0.″5 along the molecular jet (with a position angle (PA) of ∼11° (Aalto et al. 2016)), in the eastern part of a (possible) molecular disk aligned with the PA=90° stellar major axis, and also in filamentary north-western and south-eastern minor axis structures. Extended emission can be found in the molecular jet (with a total size of 3″) and in v-shaped (or an asymmetric cross) minor axis emission of opening angle θ=50°-70°. Faint emission is also found out to r=0.″6 along the stellar major axis. The CO 3–2 brightness temperatures and their interpretation in terms of gas temperatures are presented in Sec. 4.

3.2.2. Velocity field

Fig 2 shows that the CO 3–2 velocity field is complex with the highest velocities in the molecular jet which is also showing radial velocity reversals. Lower velocity shifts are seen along the stellar major axis (25 km s^{-1} east-west velocity shift (at PA=90°) observed before by Aalto et al. (2016)) and between east-west components in the narrow wind. Abrupt velocity changes from the red-shifted narrow wind to the blue-shifted jet can be seen 0.″25 to the north. This is likely evidence of dynamically separate structures overlapping along the line-of-sight. The curved feature from the southern jet to the east shows a velocity gradient with receding velocities as it connects with the narrow wind, and we also detect a velocity gradient across the northern "expansion" structure in the jet. The velocity field in the central 0.″1 has a similar PA of 140° that was found for the high frequency (690 GHz) band 9 central velocity field (Aalto et al. 2017). However, the intensity weighted moment 1 map is not sensitive to the highest velocity emission, and in Sec. 3.3.1 below we find a different PA of the velocity shift as we get closer to the nucleus.

3.2.3. Velocity dispersion and line widths

High dispersion emission (σ=40-90 km s^{-1}) is found in the nucleus and along the molecular jet out to a distance of ∼0.″25. Dispersion is generally dropping with radius in all structures. After the "expansion", the jet σ drops significantly, down to values of 8-15 km s^{-1} in the north. To the south there is a similar, but less pronounced, trend. Dispersion in the narrow wind is σ∼40 close to the nucleus, and then drops to σ=10-15 km s^{-1} after 25-30 pc. Emission of intermediate σ=10-30 km s^{-1} is generally found on size scales 0.″25 to 0.″5, and extending to the east along the stellar major axis and in the eastern part of the minor axis. A discussion of σ in terms of physical conditions and turbulence can be found in Sec. 4.

3.3. High-velocity CO 3–2 emission

3.3.1. The highest velocity gas

The highest velocity emission >160 km s^{-1}, is found in the nucleus. Red- and blue-shifted velocities of 160 km s^{-1} peak in the nucleus with a PA of ∼100° and Δx of 0.″028 ± 0.″003 (2.8±0.3 pc)(Fig. 4). The centre of this velocity shift is at ∼1730 km s^{-1} and the kinematic centre is slightly offset to the east from the continuum peak (Fig. 4). In Sec. 5.1 we discuss this velocity shift as representing a nuclear rotating disk and estimate its dynam-

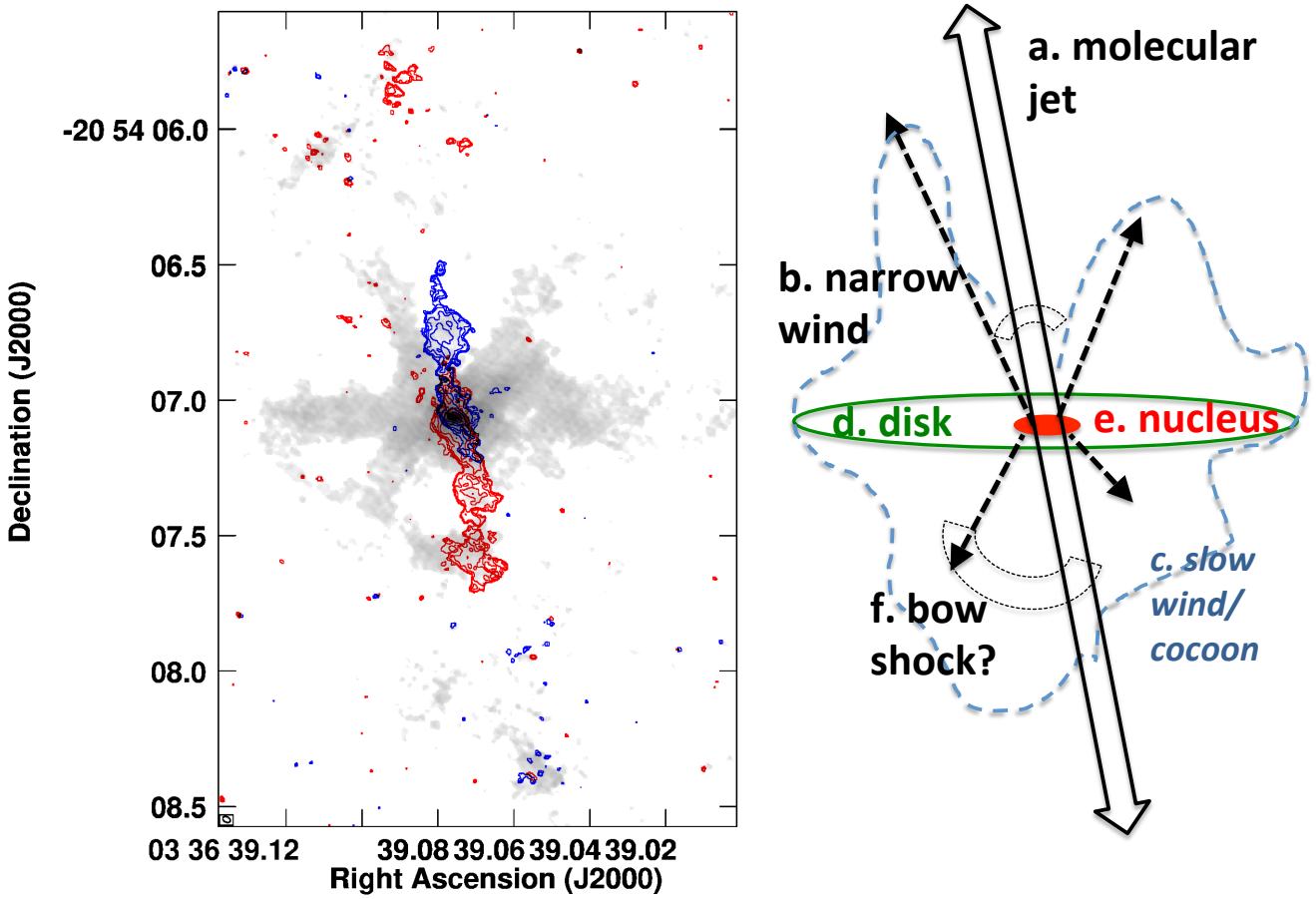

Fig. 1: Left panel: CO 3–2 integrated intensity image where emission close to systemic velocity (0-70 km s^{-1}) is shown in greyscale (ranging from 0 to 1 Jy km s^{-1}). The high-velocity (±80 to ±160 km s^{-1}) emission from the molecular jet is shown in contours (with the red and blue showing the velocity reversals). The contour levels are 6×10^{-3} ×(1,2,4, 8, 16,32,64) Jy km s^{-1} beam^{-1}. Right: Chart of the various components of the molecular structure of NGC 1377 as presented in Sec. 3.1. The outline of the slow wind (which may be a jet cocoon (Sec. 6.4)) is largely taken from the low-velocity gas in Aalto et al. (2016) since a significant fraction of he extended low-velocity gas is missing in the high-velocity data (Sec 3.2).

ical mass. We also find extensions of the high-velocity gas that can be linked to the narrow wind and jet (Sec. 7). In Fig. 4 another, blue-shifted high-velocity component is visible 2 pc east of the continuum peak. The origin of this emission is not clear, but it is difficult to assign it to any outflowing structure. It is located where the asymmetric continuum emission (Sec. 3.6) has an extension to the east.

3.3.2. The molecular jet

High-velocity gas (projected v=80-160 km s^{-1}) (Fig. 1) is aligned in a ±1.″5 (±150 pc) long, collimated, jet. It has a symmetry angle of PA=11° (Aalto et al. 2016), and the jet structure is resolved in our 2 by 3 pc beam. The jet width is 3-7 pc on average, but widens to 10-17 (Fig. 1) about 20 to 25 pc north of the nucleus. The emission remains wide for ~20 pc before narrowing again, and is also diverging from the symmetry axis of the jet. The widening and narrowing of the jet occurs further out (40 pc) to the south, but the emission departs from the symmetry axis at roughly the same distance from the centre. There is a gap in high-velocity emission along the jet until after 0.″5 where emission appears again, at the reverse velocities. In the north, the high-velocity gas becomes redshifted, and vice versa to the south. This behaviour was observed at lower spatial resolution and discussed by Aalto et al. (2016). Also, the emission close to the nucleus to the north shows wiggles on small scales.

In a precessing jet scenario (Aalto et al. 2016), there is also jet emission at lower velocity which should be further away from the jet symmetry axis. In Fig. 5 we show how the structure and width is changing with velocity, where the highest velocity gas is aligned with the jet axis, while at lower projected velocities, the emission is broader and also starts to deviate from the symmetry axis. At lower jet velocities, curved structures, roughly perpendicular to the jet axis, also become apparent. In particular to the south.

The jet is likely launched from within a small radius (Sec. 7) and potential rotation may not be resolved. In Fig. 5 panels c) and d) show redshifted collimated emission at lower jet velocities to the north (and vice-versa to the south). It is possible that this is unresolved jet-rotation, but it may also be emission belonging to the narrow wind (see below). There is a also velocity shift

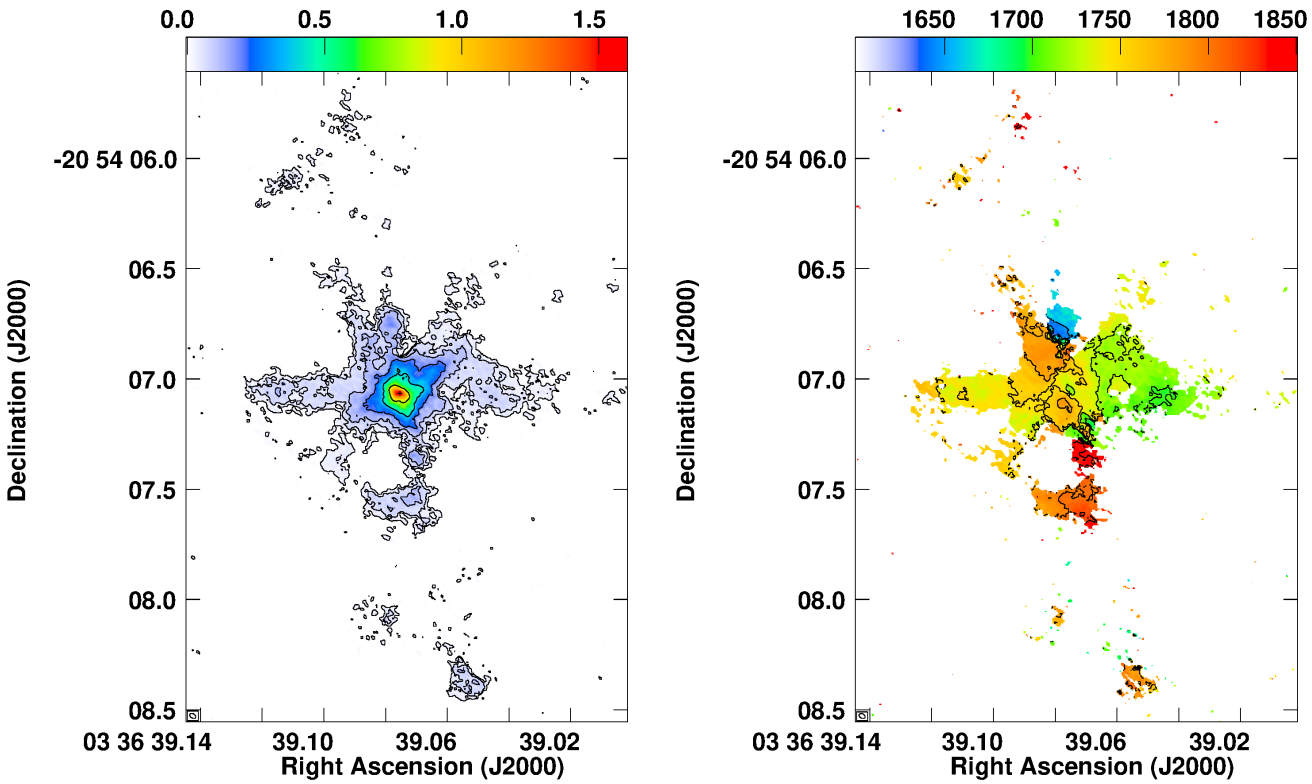

Fig. 2: Left: Integrated CO 3–2 intensity (mom0) with contours 0.017× (1, 3, 6, 12, 24, 48) Jy km s^{-1} beam^{-1}. Colours range from 0 to 1.7 Jy km s^{-1} beam^{-1}. Right: Velocity field (mom1) with contours from 1675 km s^{-1} to 1825 km s^{-1} (steps of 25 km s^{-1}), colours from 1650 to 1850 km s^{-1}. The cross indicates the position of the 345 GHz continuum peak.

(opposite to disk rotation) in the northern jet expansion which we attribute to internal working surfaces and bow shocks (see Sec. 6.4).

3.3.3. The narrow wind

In Fig. 1 the narrow wind is visible as a cross-shaped minor axis emission structure (dominated by the northern emission) of opening angle θ=50°-70°. The wind becomes apparent in panels c and d in Fig. 5 for velocities 60-110 km s^{-1}, (but is also apparent at lower velocities) and is also obvious in the moment maps (Fig 2). Higher velocity gas in the wind is also seen on small scales in the nucleus (Fig. 4). The wind has a north-south asymmetry in extent of its high-velocity component which extends only 10-20 pc to the south while low-velocity wind emission can be found on the south-eastern side down to 50 pc. On the south-western side even the low-velocity wind component is missing. To the north, the eastern component of the wind extends out to 100 pc while the western part appears to curve down towards the disk at a distance 25 pc from the centre (lower velocity gas extends out to 50 pc). The narrow wind is also not symmetric about the jet axis (eastern red component is closer to the jet than the blue). On the south side of the jet, 0.″5 from the centre, the jet connects to a lane of emission extending to the east and curving north.

A velocity shift between the east- and west part of the narrow wind is evident in Fig. 4 and in Fig. 5 (panels c and d), and appears to be consistent with rotation. Velocity shifts between the eastern (red) and western (blue) part of the wind appear to peak at ±110 km s^{-1} out in the wind, but are as high as ±160 km s^{-1} near the nucleus. In Aalto et al. (2017) we find that the 690 GHz CO 6–5 emission close to the nucleus also show the red- and blue-shifted v-shaped emission at the base of the narrow wind. In Sec. 7 we present a simple model of the wind rotation as a possible signature of a magneto-centrifugal disk-wind.

3.4. Systemic and low-velocity gas

The systemic and low-velocity gas (projected velocities 0-50 km s^{-1}) (Fig 1) consists of a bright central feature and larger scale emission extending primarily along the minor axis of NGC 1377. Some low-velocity emission is associated with the narrow wind, but most is wider and extends out to distances of 75-120 pc. The missing flux in the high resolution map (compared to the 0.″25 × 0.″18 resolution CO 3–2 map (Aalto et al. 2016)) is largely in the low-velocity gas.

Aalto et al. (2016) reported that the low-velocity emission surrounds the molecular high-velocity jet in a butterfly-like pattern. In this high resolution map the low-velocity emission that we recover is located in narrow filamentary-like structures. The low-velocity minor axis flow shows a small east-west velocity gradient (10-30 km s^{-1}) and there is also a modest north-south velocity shift of ~20-30 km s^{-1}. Low-velocity emission is also associated with the PA=90° stellar disk of NGC 1377 out to a radius of r=60-100 pc. As noted in Sec. 3.2.2, the velocity shift along this major axis is very small, ±25 km s^{-1}.

3.5. HCO^+, $H^{13}CN$ and vibrationally excited HCN

HCO^+ 4–3 emission is found (Fig. 6) in a structure with a FWHM size of 4.5 × 2.5 pc and a PA of 70° ± 10° centred on the nucleus. Kinematics are complex and not consistent with

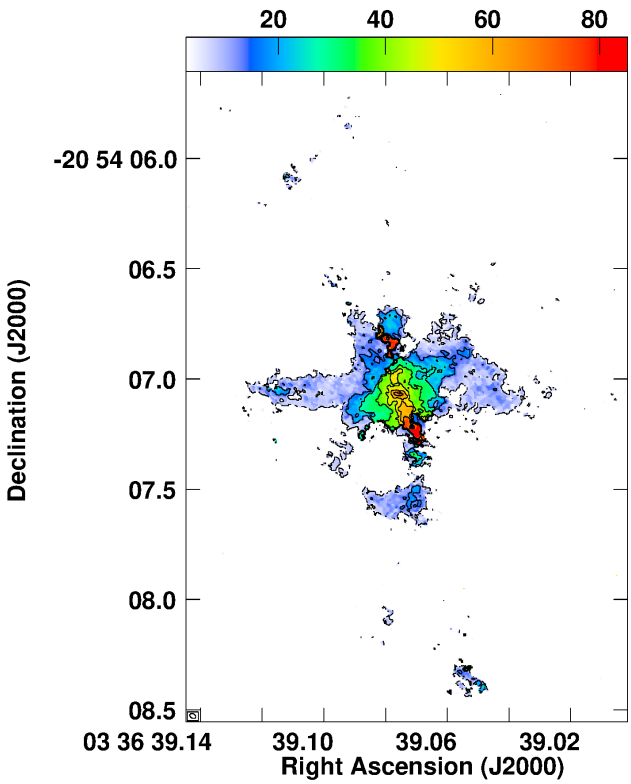

Fig. 3: Dispersion map (mom2) with contours 5×(1, 3, 5, 7, 9, 11, 13) km s^{-1}. Colours range from 3 to 85 km s^{-1}. The cross indicates the position of the 345 GHz continuum peak.

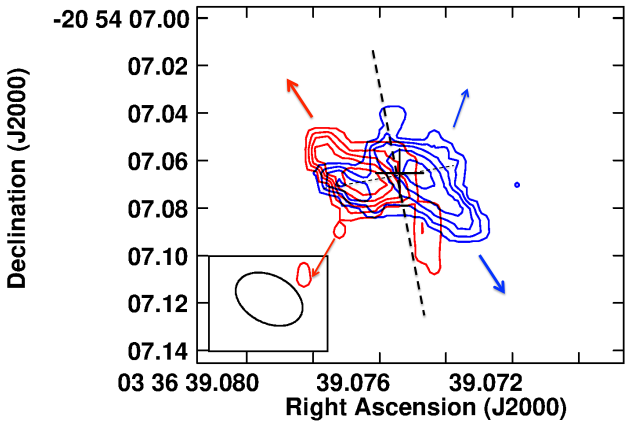

Fig. 4: Red- and blueshifted high-velocity gas: Nuclear orientation of rotation (Blue: 1552 - 1572 km s^{-1}; Red: 1886 - 1906 km s^{-1}). (Contours 0.004×(1,2,3,4,5) Jy beam^{-1} kms^{-1}). The thick, black, and dashed line indicates the jet orientation, the thin line the orientation of the nuclear velocity shift. The red and blue arrows indicate the narrow wind.

a single kinematical component. The velocity field in the centre has a similar PA of 140° as for CO 3–2 (Sec. 3.2.2). However, the intensity weighted moment 1 map is not sensitive to the highest velocity emission, and the velocity field is the result of superposed rotating and non-circular components (out- and in-

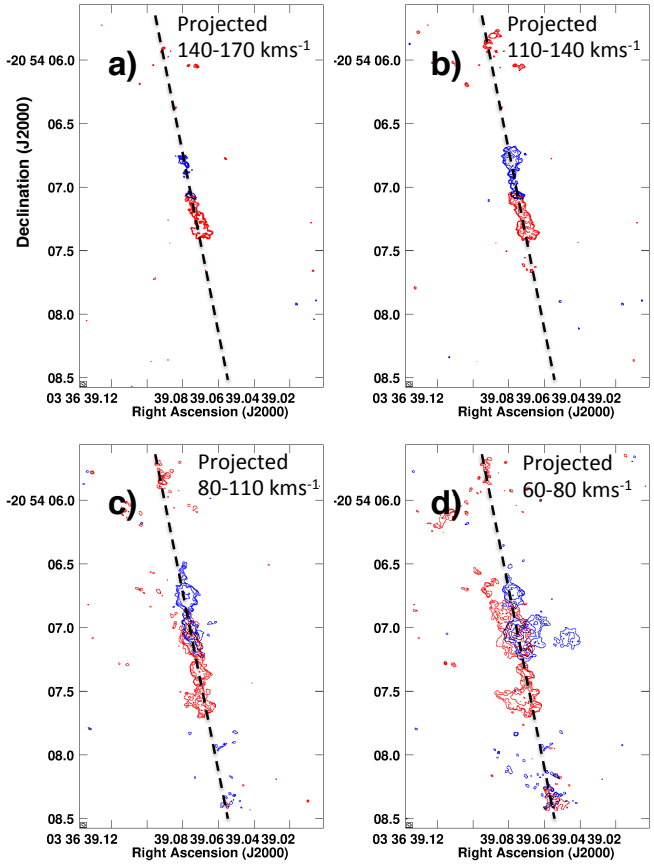

Fig. 5: Panels showing the structure of the jet at various velocity intervals: Top left panel: Highest velocity, projected velocities 140-170 km s^{-1}. Top right: High-velocity, projected velocities 110 -140 km s^{-1}. Bottom left: Intermediate velocity, projected velocities 80-110 km s^{-1}. Bottom right: Lower velocity 60-80 km s^{-1}. The black dashed line shows the orientation of the jet axis. Contour levels are (for the blue- and redshifted emission respectively): Panel a) 0.004×(1,2,3,4,5); Panel b) 0.004×(1,2,4,8,16,32); panels c) and d) 0.004×(1,5,10,20,50) Jy beam^{-1} kms^{-1}.

flows)(see Sec. 5.1). The nuclear spectrum is double peaked with a maximum brightness temperature of 40 K at v=1670 km s^{-1}.

We also detect H^{13}CN J=4–3 and vibrationally excited HCN J=4–3 v_2 = 1f (T = E_l/k=1050 K)(HCN-VIB). HCN-VIB emission is highly concentrated on the nucleus with a FWHM size of 2.0 × 1.5 pc and a PA of 66° ± 10°. The line is wide with ΔV=350 km s^{-1}(FWHM) with a peak T_B=15 K. We only have blue-shifted H^{13}CN line emission in our spectral window, but we can see that blue-shifted emission is found associated with the jet, but also with the continuum extension to the east of the nucleus (Sec. 3.6).

We also find lines at redshifted frequency v=342.26 and 344.5 GHz. The identification of these lines is not clear but we tentatively identify the first as HC^{15}N J=4–3 and the second either as vibrationally excited HC$_3$N or as SO_2. Lower resolution spectra, and a brief discussion of the line identification in the same spectral set-up, were presented in Aalto et al. (2016).

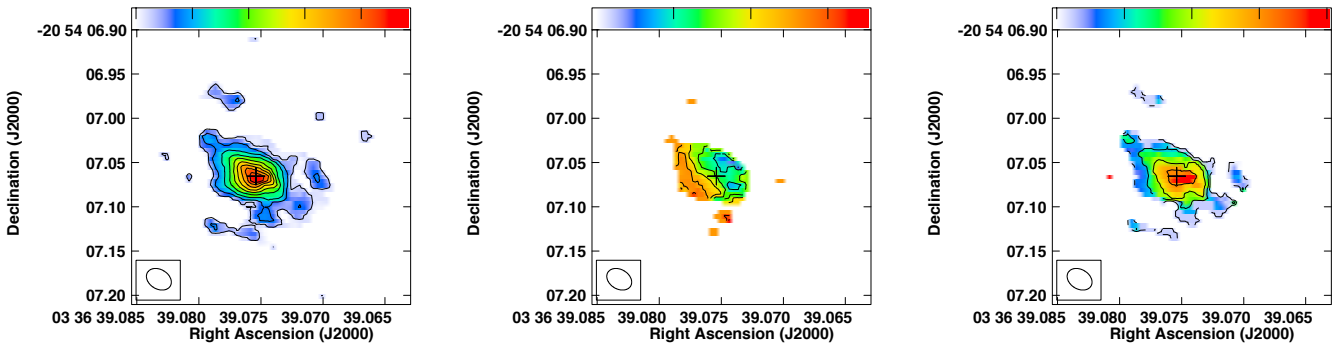

Fig. 6: HCO^+ 4–3 moment maps. Left: Integrated intensity (mom0) where contours are 0.025× (1, 3,5,7,9,11,13,15,17) Jy km s^{-1} beam^{-1}. Colours range from 0 to 0.48 Jy km s^{-1} beam^{-1}. Centre: velocity field (mom1) where contours range from 1650km s^{-1} to 1825 km s^{-1} in steps of 25 km s^{-1}, colours range from 1650 to 1825 km s^{-1}. Right: Dispersion map (mom2) where contours are 10×(2,4,6,8) km s^{-1}. Colours range from 20 to 100 km s^{-1}. The cross indicates the position of the 345 GHz continuum peak.

3.6. Continuum

We merged all line-free channels in our observations into a 0.8 mm continuum image (Fig. 7) with an rms of 30 μJy. The continuum consists of a compact component and emission extending to the east of the peak. A two-dimensional Gaussian fit gives a FWHM size of 4.1×2 pc and a position angle PA=90±5°. The continuum is faint (0.41±0.02 mJy beam^{-1} peak (T_B=5 K) and 1.3±0.1 mJy integrated). Aalto et al. (2016) report a 345 GHz continuum flux of 2.2 mJy. The missing 1 mJy is found in more extended and patchy emission, and hence not part of this Gaussian fit. The PA of the high resolution continuum differs from that at lower resolution, which has a PA of 104° (Aalto et al. 2016). Based on the radio observations of Costagliola et al. (2016), we estimate an upper limit to the contribution from synchrotron and free-free emission to the 0.8 mm continuum of 3% and 6% respectively.

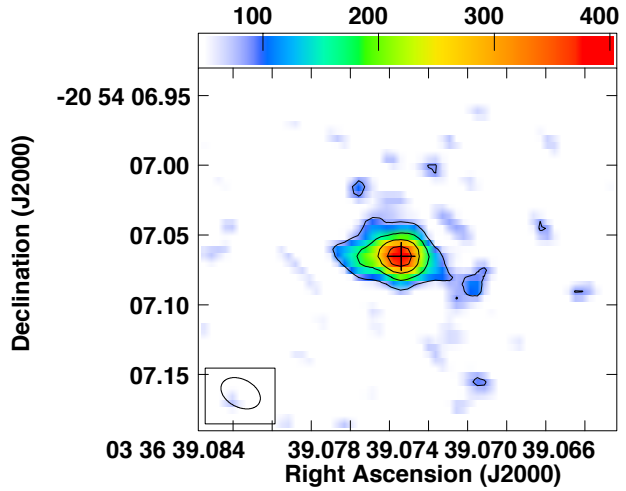

Fig. 7: 0.8 mm continuum (merged 342, 349, 356 GHz line-free channels). Contour levels are 0.085 ×(1,2,3,4) mJy beam^{-1} and colours range from 0.05 to 0.4 mJy. The lowest contour is at 3σ. Coordinates are in J(2000)).

4. Physical conditions

4.1. Gas and dust temperatures

The high resolution of our ALMA observations allows us to measure meaningful CO 3–2 brightness temperatures (T_B(CO 3–2)), which can be used as a lower limit to the gas kinetic temperature (T_k). Gas with high T_k ($\gtrsim$100 K) is located in the inner r=4 pc in a complex structure. The maximum T_B(CO 3–2)=180 K is found at a velocity v=1700 km s^{-1}, blueshifted from v_{sys} and located 0.″02 north of the nuclear continuum peak. The orientation and major/minor axis ratio of the high-T_B(CO 3–2) emission is similar to that of the 0.8 mm nuclear continuum (see Sec. 3.6). Furthermore, the detection of emission from the polar molecule HCO^+ 4–3 implies that gas volume densities, n, are large enough (n>10^4 cm^{-3}) to couple dust and gas (Sec. 3.5). We can therefore assume that T_d~T_k and that T_d >100 K in the central region, and T_k=T_d~180 K in the inner 3 pc.

The CO 3–2 emission in the jet is clumpy with varying T_B(CO 3–2). Brightness temperatures reach T_B(3–2)=40-50 K in the high-velocity gas at r~25-40 pc to the north and south of the nucleus. This is also the region where the jet appears to widen before narrowing again further out. Such elevated gas temperatures in the expansion region may indicate local heating from shocks.

Closer to the nucleus, r=10-20 pc, T_B(CO 3–2) is 20-25 K in the high-velocity gas while higher values, T_B(CO 3–2)>50 K, are found for lower velocities in the jet and narrow wind. Interestingly, the nuclear emission of the more highly excited CO 6–5 emission is associated with the jet (and the northern narrow wind) while the inner CO 3–2 emission has a higher PA more similar to that of the disk. The difference in uv coverage between the CO 6–5 and 3–2 observations means that comparisons are precarious, but the difference in nuclear morphology is striking (Aalto et al. 2017). Bright, near-systemic (v~1740 km s^{-1}), collimated CO 6–5 emission extends 10 pc to the south of the nucleus, while this structure is missing both for CO 3–2 and HCO^+ 4–3. This is either because of self-absorption masking emission at v=1740 km s^{-1}or because the nuclear jet component is hot and dense with elevated CO 6–5/3–2 intensity ratios. In general only very little HCO^+ 4–3 emission is associated with the jet (or wind) outside the nuclear launch regions.

In the gas aligned with the stellar disk, warm (T_B(CO 3–2)~50 K) gas is found in the inner 0.″2. Further out values drop to 20-30 K.

4.2. Velocity dispersion and turbulence

High values of σ in the jet (Fig. 3) are due to emission with high intrinsic velocity width and, in some locations, also to overlapping multiple, narrower emission features along the line-of-sight. The elevated intrinsic dispersion (σ=40-60 km s^{-1}), is found from the nucleus out to the jet expansion at r~25-40 pc. Position-velocity (pV) diagrams across the jet axis (Fig. 8) show that σ in the wind (narrow and slow) is lower than that in the jet. Some of the large line widths in the jet may stem from expansion or unresolved rotation. However, velocity dispersions in the jet and wind are still very high by comparison to normal giant molecular clouds or cloud cores on similar size scales. Therefore, standard CO luminosity to H_2 mass conversion factors are unlikely to apply (see Sec. 6). The turbulent jet and wind of NGC 1377 are also unlikely sites of ongoing star formation, a possible scenario suggested for other galactic-scale outflows (Maiolino et al. 2017).

The origin of the large line widths may be internal working surfaces from variable jet emission or linked to jet driving processes (see Sec. 6.4).

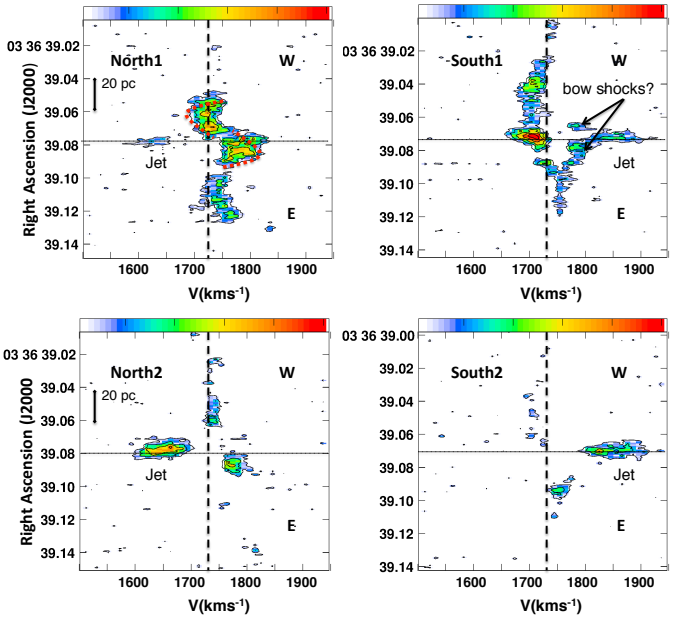

Fig. 8: Position-velocity (pV) diagrams of CO 3–2 across the jet axis. Contour levels are 0.6×(1,2,3,4) mJy beam^{-1}, and colour range from 0.6 to 30 mJy. The horizontal dotted line indicates the jet symmetry axis. Top left panel: cut 0.″15 to the north of the nucleus. The expected signature of a rotating wind is indicated with red dashed curves (see Fig. 12 and Sec. 7.1.1). Lower left panel: cut 0.″3 to the north of the nucleus. Top right panel: cut 0.″15 to the south of the nucleus; Lower right panel: cut 0.″3 to the north of the nucleus. The arrows point to structures that are proposed to be bow shocks (see Sec. 6.4).

5. Nuclear gas and dust properties

5.1. Nuclear morphology, dynamics, and enclosed mass

The SMBH of NGC 1377 appears obscured by an asymmetric disk or torus of dimensions r≃4 pc for CO 3–2, r≃2 pc for HCO$^+$, and r≃1 pc for HCN-VIB. The presence of a nuclear warp is supported by changing position angles (PA) on different

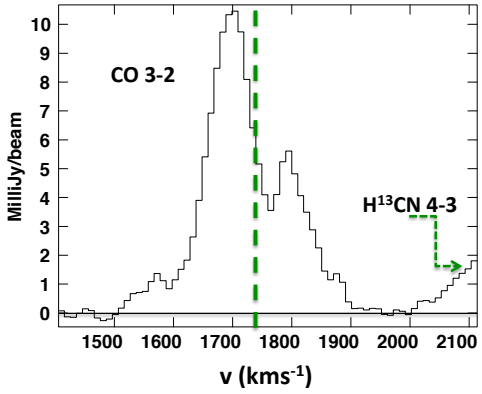

Fig. 9: Nuclear spectrum of NGC 1377 showing the asymmetric line profile of CO 3–2 (there is an H^{13}CN 4–3 feature to the right). The green dashed line indicates systemic velocity.

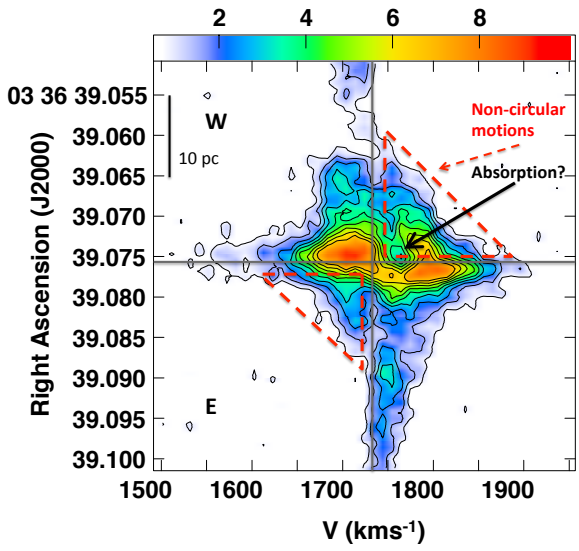

Fig. 10: CO 3–2 pV diagram cut across PA=90° along the nuclear major axis. Red dashed triangles show regions of non-circular velocities. The arrow indicates the potential absorption structure on the nucleus and to the west.

size scales. From a PA of 104° for the 0.8 mm continuum on scales of 20 pc (Aalto et al. 2016) to PA=90° on scales of 4 pc. The difference in orientation of the launch region between the jet and the narrow wind, also supports the scenario of a complex nuclear warp. Furthermore, the lower PA of the HCN-VIB emission (excited by high surface brightness mid-IR dust emission (Sakamoto et al. 2010; Aalto et al. 2015b)) implies that polar hot dust may also contribute to the obscuration of the nucleus. This has also been suggested for other galaxies, for example the nuclear obscuration in the Seyfert galaxy Circinus (e.g. Tristram et al. 2014; Izumi et al. 2018).

The dimension and physical conditions of the NGC 1377 torus is similar to those of other torii imaged at high resolution so far (e.g. García-Burillo et al. 2016; Impellizzeri et al. 2019; García-Burillo et al. 2019; Combes et al. 2019). The H_2 column density does however appear to be higher in NGC 1377 on similar scales: The core component of the 0.8 mm continuum has a brightness temperature of ~5 K. For T_d=180 K the dust opacity at λ=0.8 mm is τ≃0.04. Using the formalism of Keene et al.

(1982) $N(H + H_2)/\tau_\lambda = 1.2 \times 10^{25} (\lambda/400\mu m)^2$ cm^{-2}, we find a $N(H + H_2) \simeq 1.8 \times 10^{24}$ cm^{-2}. This suggests that there might be a Compton Thick (CT) dust structure with radius $r \simeq 1.5$ pc around the NGC 1377 nucleus. The column density is higher than that previously estimated from the 690 GHz continuum for a larger (5 pc) beam (Aalto et al. 2017), but is consistent for the smaller radius found for the 0.8 mm continuum. However, if the dust is actually hotter than T_d=180 K, then 1.8×10^{24} cm^{-2} is an upper limit to $N(H + H_2)$. We exclude contributions from synchrotron and free-free to the 0.8 mm continuum emission due to the extreme radio-quietness of NGC 1377 (Costagliola et al. 2016), but this requires further investigation.

The nuclear high-velocity gas appears to be in Keplerian rotation with a PA of 100° (Sec. 3.3.1). The actual inclination of the nuclear gas is difficult to determine and is likely changing with radius due to the suggested presence of a warp. The high resolution 0.8 mm continuum implies a nuclear inclination $i \gtrsim 60°$ suggesting a dynamical mass M_{dyn} of 0.9×10^7 M$_\odot$. To this we added the uncertainty in position of the nuclear high-velocity gas discussed in Sec. 3.3.1, and the possibility that the inclination could be higher, which results in $M_{dyn} = 9^{+2}_{-3} \times 10^6$ M$_\odot$.

This M_{dyn} is higher than previously estimated enclosed masses for NGC 1377 (Aalto et al. 2012, 2016, 2017) and we attribute this to the higher sensitivity and resolution of the new CO 3–2 observations. Rotational velocities can be separated from non-circular motions to a higher degree than before. At such small radius M_{dyn} is expected to be dominated by the SMBH and the high mass is interesting since it is above the value suggested by the $M - \sigma$ relation (e.g. Graham et al. 2011). This is discussed further in Sec. 9.

An additional blue-shifted high-velocity component is seen on the red side of nuclear rotation (Fig 4). If real, this may be an in- or outflowing gas component, or it is linked to a second nucleus. A binary SMBH is a tantalizing scenario in the context of NGC 1377 as a merger remnant. Two SMBHs could drive jet-precession or, with different inclinations of the disks, do away with the need for jet precession to explain the velocity reversals. Further studies at higher resolution are necessary to further investigate the possibility of a binary SMBH.

The PA of 100° for the nuclear dynamics is different from the previously suggested orientation of nuclear rotation. In Aalto et al. (2017) the CO 6–5 high-velocity gas has an apparent PA of 140° ± 20°, but the CO 6–5 velocities are a factor of two lower than the high-velocity gas traced with our new CO 3–2 data. We do find this dynamical component (70 - 80 km s^{-1}) in the moment 1 maps of CO 3–2 and HCO$^+$ 4–3. We propose that this intermediate velocity gas is part of the wind and jet rather than the nuclear disk (see Sec. 7).

5.2. Indications of inflowing gas

The CO (Fig. 9) and HCO$^+$ spectra are double-peaked in the centre, with maxima at velocities: ~1670-1700 km s^{-1}and ~1800-1810 km s^{-1}. CO 3–2 and HCO$^+$ 4–3 emission avoid the location of the dust continuum peak at velocities near systemic. The continuum is too faint to cause the depression of the systemic CO and HCO$^+$ emission, which is either the result of a dynamical structure or self-absorption in lower-excitation foreground gas. The latter is a more likely scenario since the double peak is not seen in HCN-VIB (probing high column density hot gas (e.g. Aalto et al. 2015a)) and the dust continuum peak is also consistent with large gas column densities here.

The (potential) absorption depth peaks at velocity 1760 km s^{-1}, ~20-30 km s^{-1}redshifted of systemic. It may indicate that lower excitation foreground gas is moving in towards the centre of NGC 1377, possibly originating in the envelope of gas that may be fed by the slow wind (e.g. Evans 1999) (see also (Sec. 6.4)). The position velocity (pV) diagram (Fig. 10) shows the purported absorption feature occurring mostly west of the nucleus, on the "forbidden" side of non-circular motions. However, we caution that the interpretation of the dynamical origin of gas in absorption features is complex.

The pV diagram also reveals emission at non-circular velocities, starting 10-15 pc from the nucleus on both sides of the centre, although there is an asymmetry with stronger emission on the western side. This emission may also be attributed to fast inflowing gas. Models of rotating inflows predict similar velocities to the Keplerian at these distances from the central object, although the radial dependence is different than Keplerian (e.g. Oya et al. 2014). However, given the combined presence of a nuclear warp and disk-wind it is likely that we see overlapping structures of inflow and outflow, that are difficult to disentangle.

The gravitational (Bondi) radius of influence of a 9×10^6 M$_\odot$ SMBH (with stellar velocity dispersion σ=83 km s^{-1} (Aalto et al. 2012)) is $r_g \simeq 4$ pc. Hopkins et al. (2012) suggest that near r_g, systems become unstable to the formation of lopsided, eccentric (m = 1 mode), precessing gas+stellar discs. Strong torques induces shocks and inflows, which may in turn help drive outflows. The dimensions of the nuclear disk in NGC 1377 are similar to the expected size of the SMBH radius of influence.

5.3. Accretion luminosity or compact star formation

To estimate the luminosity of the nuclear dust structure we adopt the same method as Aalto et al. (2017). Fitting the luminosity to a simple spherical dust structure with the average radius of r=1.5 pc and T_d=180 K results in $L_{core} \simeq 4.8 \times 10^9$ L$_\odot$[1]

If the luminosity is emerging from an embedded starburst, an ensemble equivalent to $\sim 5 \times 10^3$ O-stars (with a luminosity of 10^6 L$_\odot$ each) could produce the luminosity. The approximate total mass of such an ensemble of O-stars is 5×10^5 M$_\odot$ and for a normal Salpeter initial mass function (IMF) the mass in low mass stars would be ten times that of the O-stars, resulting in a total mass in starburst stars of 5.5×10^6 M$_\odot$. This is within the allowed range of the dynamical mass[2].

However, to bury the emission from the stars of a starburst in the obscuring disk would require a very small radius ($r < 0.6$ pc to allow for enough obscuration) of the stellar distribution. This is much smaller than typical sizes of stellar clusters of this mass (2-10 pc) and the stars have to be packed extremely close. In addition, the spectrum of the faint radio emission detected has a synchrotron spectrum (Costagliola et al. 2016) which does not suggest free-free emission from a hot plasma irradiated by massive young stars.

If the luminosity is instead emerging from the accretion onto an SMBH, there is no need to add a young starburst population to the nuclear mass, and $M_{SMBH} = 9 \times 10^6$ M$_\odot$. The Eddington luminosity of the SMBH is approximately 2.7×10^{11} L$_\odot$ and the growth of the NGC 1377 black hole would occurs at a rate of ~2% Eddington to produce the luminosity.

[1] This is a factor of 4 higher than the relatively larger, but cooler nuclear dust structure suggested in Aalto et al. (2017).

[2] We are excluding a contribution from a pre-existing nuclear stellar cluster (NSC) due to the small dimensions of the nuclear dust structure.

6. Energetics and turbulence of the jet and wind

6.1. Molecular masses

Adopting a standard, Galactic CO-to-H_2 conversion factor, X(CO) the molecular mass in the jet is estimated to 2.3×10^7 $M_\odot$ (Aalto et al. 2016)[3]. However, Aalto et al. (2015c) found that a Galactic X(CO) overestimates the mass in turbulent outflowing gas by a factor ~5. Applying this factor, we instead find a jet gas-mass of $M_{\rm jet}\simeq5\times10^6$ $M_\odot$ (not corrected for any missing emission at lower velocities). For the narrow wind (NW) we estimate a mass of $M_{\rm NW}\simeq8\times10^6$ $M_\odot$, also by applying the lower X(CO) for turbulent gas. Half of the flux of the slow wind (also referred to as the envelope or cocoon (Sec. 6.4)) (SW/C) emerges from outside the turbulent region and we estimate its mass to $M_{\rm SW/C}\simeq1.8\times10^7$ $M_\odot$. Also in the disk about 50% of the emission is turbulent, resulting in $M_{\rm disk}\simeq5.5\times10^7$ $M_\odot$. These numbers have significant uncertainties and a study of the size-linewidth relation for the clouds in NGC 1377, should provide a better estimate of the cloud stability spectrum and the X(CO) of the various phases of the molecular gas in NGC 1377.

6.2. Outflow velocities

6.2.1. Wind velocity

Velocities found in the narrow wind can be >80 km s^{-1} above systemic (a combination of projected rotation and outflow motions). Comparing north and south average wind velocities, a projected outflow speed of the narrow wind is ~30 km s^{-1}. Assuming an average inclination i=70° of the launch region, the $v_{\rm out}$ of the narrow wind is 90±30 km s^{-1} (uncertainties stem from inclination, opening angle and that $v_{\rm out}$ varies with radius). The slow wind has projected outflow velocities in the range of 0-20 km s^{-1} ($v_{\rm out}$=0-60 km s^{-1}).

6.2.2. Outflow velocity of a precessing jet

The jet velocity switches from blue-to-red to the north, and vice versa to the south, which were previously interpreted as evidence of jet precession by Aalto et al. (2016). A simple model with a precession angle $\theta_{\rm p}$=10°-25° and jet outflow velocities $v_{\rm out}$=240 to 850 km s^{-1} can reproduce observations. The outflow velocity estimates are highly dependent on $\theta_{\rm p}$ and the inclination of the jet with respect to the plane of the sky. As pointed out by Aalto et al. (2016), the north and south are relatively symmetric in velocity which suggests that the jet symmetry axis is close to the plane of the sky. Deviations from the jet symmetry axis are apparent, but determination of $\theta_{\rm p}$ is difficult since the lower velocity jet emission blends in with the slow wind, and jet-wind interactions distort the symmetry. In addition, the jet emission appears patchy and is likely episodic. However, an assessment of off-symmetry jet-emission in Fig. 11, gives $\theta_{\rm p}\simeq15°$. For this $\theta_{\rm p}$ the jet may be a maximum of 2° away from the plane of the sky to fit the observed velocity reversals. A $\theta_{\rm p}$=15° implies a jet $v_{\rm out}$ of ~600 km s^{-1} (±60 km s^{-1}to account for uncertainties in the projected velocity). In this simple scenario it is assumed that the jet velocity is dominated by outflowing motions and that the element of rotation is small (Sec. 7.3). The jet emission is changing direction with time, but it is possible that these variations are not caused by a smooth "swirling" of the jet, but by more sudden, directional changes caused by an uneven accretion flow. The driving force behind the jet precession will be discussed in a future study.

[3] for gas moving at higher (projected) velocities than 60 km s^{-1} which would include >70% of the volume if the jet is smoothly precessing.

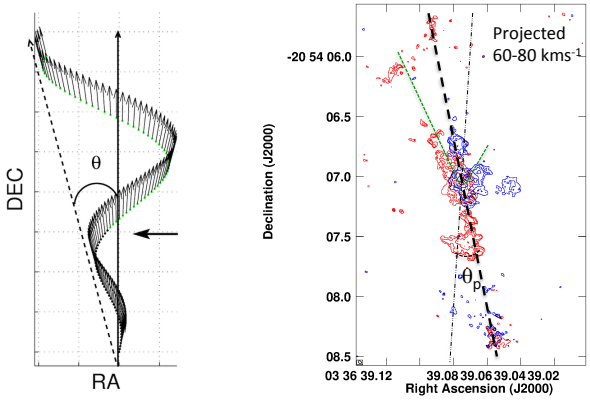

Fig. 11: Left: Schematic of the simple precession model by Aalto et al. (2016) showing the precession angle θ. Right: Lower velocity (60-80 km s^{-1}) jet emission (from Fig. 5). Contour levels are (for the blue- and redshifted emission respectively) 0.004×(1,5,10,20,50) Jy beam^{-1} kms^{-1}. The thick black dashed line shows the orientation of the jet axis. The narrow wind is outlines in green and the suggested precession angle in a thin, dashed line

6.3. Kinetic and gravitational energy

In Table 2 we list approximate estimates of the systems kinetic and gravitational energy (on scales of r~100 pc) together with the velocities for the various components. If the gravitational energy of the system is large enough, the rotating and infalling material could be converted to the outflow energy aided by a magnetic field. The kinetic energy is dominated by the jet and the gravitational energy by the stellar and gas envelope component. There is rough equipartition between the two, which may indicate a dynamical link. The driving of the jet and wind is discussed in Sec. 7.

The turbulence is high throughout the inner 50-60 pc of NGC 1377 and there is enough kinetic energy in the jet to drive the turbulence in the inner part of NGC 1377 (for jet $v_{\rm out}$ down to 120 km s^{-1}). A potential link between the jet and its surrounding is discussed in Sec. 6.4.

6.4. Bow shocks and jet-wind interactions

Simulations of jets with directional changes, and with varying jet velocity, show that the jet has transverse extensions arising from the presence of bow shock wings trailing behind each internal working surface. This produces laterally extended emission of lower radial velocities than the jet beam (e.g. Raga et al. 2001). This can be seen in the NGC 1377 molecular jet in several locations: In Fig. 5 (the panel with projected velocities 80-110 km s^{-1}) curved, blue-shifted bow-shock structures are particularly apparent 1″to the south, and a prominent redshifted curved structure at 0.″5. In the lower velocity panel (projected velocities 60-80 km s^{-1}) these curved structures widen and it is more clear that they are predominantly found on the eastern side of the jet axis. Tafalla et al. (2017) observed and modelled velocity gradients across bow-shock regions in terms of expanding "disks" of laterally ejected material. Such a velocity shift is apparent in

Table 2: Kinetic and gravitational energy

Component	Velocity (km s^{-1})	σ (km s^{-1})	K^a	W^a
Jet	600	30-60	11.2	0.01
NW	90	30	0.4	0.03
SW/C	30	10	0.2	0.03
Disk	27	10-30	0.3	0.80
BH				0.03
Stars				17
Total^b			~12	~18

[a] The kinetic energy is $K \simeq \frac{1}{2} M(v^2 + \sigma^2)$ where M is the mass of the component (jet, NW=narrow wind, SW/C=slow wind (also the envelope or cocoon), disk), v its velocity and σ its dispersion. In units of $\times 10^{11}$ M$_\odot$ (pc/Myr)^2. For the SW/C we assume an average outflow velocity of 30 km s^{-1}. The rotational velocity of the disk is assuming an i=70°. The gravitational energy is $W \simeq G\frac{M^2}{r}$ where M is the mass of the component. Units are 10^{11} M$_\odot$ (pc/Myr)^2. W_{BH} is the gravitational energy of the central SMBH inside r_{env}=100 pc and W_{star} is that of the stellar and envelope system for the same region. The mass of the stars inside r=100 pc is estimated to 2×10^8 M$_\odot$ from an HST H-band image (HST program GO14728, J Gallagher PI).
[b] The total kinetic energy of the system $K_{\rm total}=K_{\rm jet}+K_{\rm wind}+K_{\rm disk}$ and the total gravitational energy of the system $W_{total}=W_{\rm jet}$ + $W_{\rm env}$ + $W_{\rm disk}$ + $W_{\rm BH}$ + $W_{\rm star}$ out to a radius r=100 pc.

the northern widening of the jet emission (Fig. 3. (There are also smaller scale wiggles in the jet structure (seen in the first portion of the jet out to about 20 pc) that are possible results of helical kink instabilities in the jet (e.g. Todo et al. 1993).)

In the pV diagrams across the jet (Fig. 8 (in particular panel "South1")) the expected signature of the trailing, extended and lower velocity bow shock wings can be seen. The signs of bow shocks and the knotty, clumpy appearance of the molecular jet are possible signatures of internal working surfaces. Furthermore, working surfaces also arise from the interaction between jet and wind material, which is particularly complex and broad if the jet is changing direction. The more prominent bow-shock structures to the south-east may be due to the presence of more molecular material here, compared to the corresponding north-western side which appears vacated of gas (see e.g. Fig. 1). Tabone et al. (2018) discuss jet-wind interactions and how a disk-wind may refill v-shaped regions emptied by jet bow-shocks. Located north-west of the jet may be a such a bow-shock cavity which the disk-wind currently has not filled. The jet cocoon (left behind by the leading working surface) produces a low-velocity emission component that can be very extended. It is possible that the slow, wide-angle emission component that surrounds the jet and narrow wind is such a cocoon.

7. Origin and driving of wind and jet

7.1. Driving mechanism of the narrow wind - a potential rotating magneto-centrifugal wind.

In Aalto et al. (2016) a scenario where the jet is entraining and accelerating a very slow, wide-angle minor axis molecular outflow was preferred over a direct-driven wind. Here, with our new high resolution data, we can resolve the dynamics of the narrow wind and also trace it back to the nuclear disk while the slow wind is more extended and diffuse. In contrast to our previous conclusion, we now suggest that the narrow wind is primarily direct driven and that it is launched from the nuclear disk as a rotating disk-wind.

The narrow wind shows an east-west velocity shift (Sec. 3.3.3) which is consistent with the rotation of the nuclear disk. Winds and outflows can be magneto-centrifugally driven, powered by rotation and gravitational energy and launched along magnetic field lines. In this scenario, a large-scale poloidal magnetic field threads the disk in the vertical direction. When they are driven from the inner edge of the disk they are often referred to as X-winds (e.g. Shu et al. 1995), and when they are launched from further out (involving a larger section of the disk) they can be referred to as a disk-wind (e.g. Pudritz & Banerjee 2005). Magnetohydrodynamic (MHD) outflows are launched from rotating sources, the rotation of the jet and outflow is an expected feature of MHD jet and outflow formation. If a wind is emerging from the centre of a rotating disk, the outflow material is ejected with a significant amount of angular momentum, which may become conserved along the streamlines. In contrast to thermal winds, for example, MHD winds not only remove mass from the disk, but also exert a torque and remove angular momentum from the disk.

There needs to be sufficient free electrons mixed in with the molecular gas to anchor the magnetic field. The presence of emission from molecular ions (HCO^+) in the inner region of NGC 1377 is an indirect measure of the ionisation degree. The abundance of cosmic rays is for example found to be similar to that of HCO^+ when CO is not depleted (Caselli et al. 2002). Assuming that the vertical magnetic field is in equipartition with the total pressure (e.g. Ferreira & Petrucci 2011; Vollmer et al. 2018), the launch conditions for an MHD wind in the inner few pc of NGC 1377 require a B field of a few mG. This is a similar to field-strengths found in the central region of dusty galaxies (McBride et al. 2015; Yoast-Hull & Murray 2019). However, independent measurements of the magnetic field are still missing for NGC 1377.

7.1.1. An illustrative model

To illustrate how a magneto-centrifugally driven wind may appear, we have modelled a simple rotating wind emerging from a disk with outflow velocity $v_{\rm out}$ linked to the Keplerian rotational velocity $v_{\rm K}$ as $v_{\rm out}=av_{\rm K}$ (Fig. 12). In our model we have selected a to be unity, but how the outflowing wind speed is related to the disk rotational velocity is more complex and requires modelling to be determined. Studies indicate lower values of a of 0.15-0.3 (e.g. Ostriker 1997; Ferreira et al. 2006; Hone et al. 2017) at least as long as the distance from the disk is below the Alfvén surface Cabrit et al. (1999). Right above the disk, the outflow velocity is expected to be dominated by the toroidal (rotational) component, while the poloidal component is expected to dominate beyond the Alfvén surface.

The illustrative example in Fig. 12 is idealized and does not include a molecular jet component or extended gas. However, it's structure can be compared to the inner part of the narrow wind. The wind-rotation is clear in Fig. 2, and in the panels c and d in Fig. 5. Here it is also evident that the counterpart to the north-eastern red wind-component is missing on the blue side to the south-west. Wind-rotation signatures are lost to the south sooner than to the north. In Fig. 8 we have marked the expected

signatures of the rotating wind in the 0.″15 transversal cut across the jet.

7.1.2. Other, or auxiliary, wind-driving mechanisms

The momentum flux of the narrow wind, $\dot{M}v{\sim}7L/c$, is higher than expected for a radiation pressure driven flow and the relatively low opening angle (50° - 70°) is more consistent with an MHD wind (Ouyed & Pudritz 1997). However, we cannot exclude that radiation pressure is providing auxiliary driving. Scenarios of radiation-pressure aided MHD jets and winds for cold disks have, for example, been discussed by Cao (2012) (see also Vollmer et al. (2018)). Since the inner region of NGC 1377 is very dusty it is primarily radiation pressure from dust that should be important. The misalignment between the jet and narrow wind results in jet-wind interaction (Sec. 6.4). Therefore, even if the wind is direct driven, the jet impacts it and is a possible source of turbulence.

The wind launched from the torus of NGC 1377 resembles to some extent the outflowing torus seen in NGC1068 (García-Burillo et al. 2019) where a hot AGN wind is entraining molecular gas in the torus. The torus may collimate the hot wind which would then entrain cold molecular gas. There is also the radiation-driven fountain model (Wada 2012) where an AGN-powered dusty outflow, a failed wind, and an inflow, form a dusty hollow cone. However, there is currently no evidence for the presence of a hot ionized wind, at least not emerging from the inner region of NGC 1377, nor is there any evidence of a supernova driven wind (Costagliola et al. 2016). Roussel et al. (2006) suggest that most of the ionizing photons in the inner region of NGC 1377 are deeply buried. They do not detect any optical [O III], [O II], or Hβ emission and infer that [N II] and [S II] emission arise in the foreground. Roussel et al. (2006) propose that a nascent (<1 Myr) starburst is embedded at the core of NGC 1377. We cannot exclude that star formation is occurring inside the opaque nuclear dust core, but there is no indication that it has enough power to drive the jet and narrow wind of NGC 1377.

More multi-wavelength studies of the inner region of NGC 1377 are necessary to determine the true nature of the buried activity and the launch and driving mechanism of the wind. Here we suggest that the narrow wind is primarily a magneto-centrifugal wind aided by radiation pressure, and that its structure and turbulence transmission is impacted by jet-wind interactions.

7.2. Driving of the slow wind

As discussed in Sec. 6.4, the slow wind may have formed from the leading- and internal working surfaces of the jet. The slow gas has the expected pV diagram behaviour of a jet cocoon (Sec. 6.4) producing an envelope of gas. It is also possible that that star formation outside the dusty nucleus may occur and can help drive feedback in NGC 1377. One example of such a scenario is the enshrouded luminous infrared galaxy NGC 4418. An optical study suggests the presence of a kpc-scale dusty superwind, disconnected from the embedded nuclear activity (Ohyama et al. 2019). A large-scale superwind in NGC 1377 is unlikely to drive the narrow wind or the molecular jet, but may potentially impact the slow wind.

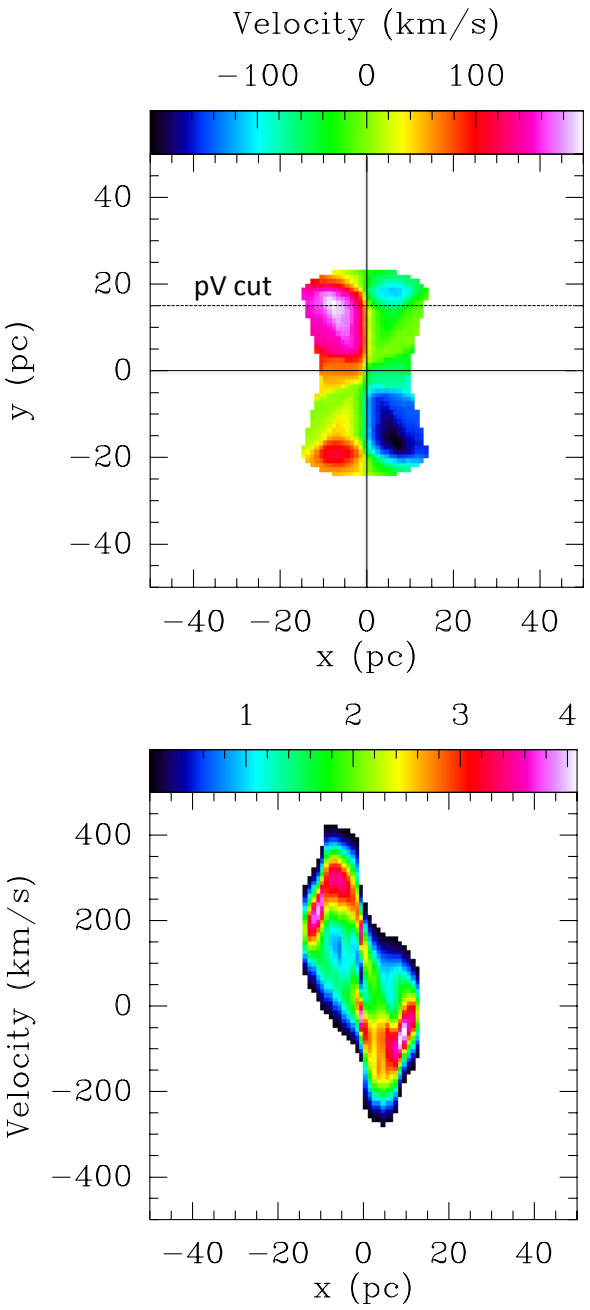

Fig. 12: Simple, illustrative model of a rotating disk-wind. In this example, we assume a uniform nuclear disk of inclination i=70° in Keplerian rotation (v_K) in response to an SMBH of mass 7×10^6 $M_\odot$ and a negligible disk mass. We let the outflow velocity $v_{out}=av_K$ with a=1. We restrict the disk radius to r=20 pc and do not include the molecular jet in the model. We let the wind have an inclination to the rotating disk of ϕ=25° giving the wind an opening angle of 50°. The structure is "observed" with a resolution of 1 pc. Top panel: Model moment 1 (velocity field) map showing the resulting rotating wind. Lower panel: Model transversal pV cut at a distance 0.″15 from the centre.

7.3. Jet driving mechanism

Aalto et al. (2016) discussed several possible scenarios for driving the molecular jet: i) entrainment by a very faint radio jet, ii) gas accretion into the SMBH or onto nuclear disk, iii) radiation pressure from dust, or iv) a starburst wind. The two latter scenar-

ios seem less likely since it is difficult to explain the extremely collimated structure in a radiation pressure powered wind and there is not enough power in star formation.

An estimate of the momentum flux of the jet ($\dot{M}v$) is $\sim 37L/c$ (using the conservative estimate of $M(H_2)$) which is much higher than expected for radiation pressure driven flows, but consistent with values found for AGN-powered and jetted outflows (e.g. Feruglio et al. 2010; García-Burillo et al. 2014), and also for protostellar feedback in the earlier stages of evolution (e.g. Bontemps et al. 1996). There are several examples of molecular gas being entrained by an AGN-driven radio jet. The gas is shocked and heated by the jet, and in some cases, also carried out of the galaxy. It is also not uncommon for the nuclear accretion disk to be misaligned with the host galaxy and the radio jet therefore propagating through its disk (e.g. Matsushita et al. 2007; García-Burillo et al. 2014; Morganti et al. 2015; Dasyra et al. 2015). So far, for cases where a radio jet is entraining molecular gas, it is found that the gas is lining the radio jet, in contrast to the case for NGC 1377, where the cool molecular gas occupies the spine of the jet. In addition, no radio-jet has been found in NGC 1377 which is one of the most radio-quiet objects in the sky. This suggests that the molecular material may represent the primary ejected material in NGC 1377. Such scenarios have been discussed and modelled by Panoglou et al. (2012).

If the molecular jet is not entrained by a radio jet it may in itself be an MHD disk-wind powered by accretion onto the circumnuclear disk. The rough equipartition between gravitational and kinetic energies in the system (Sec. 6.3) is consistent with the notion of an outflow powered by gravitationally driven inflow on scales of 100 pc down to <1 pc. The envelope (a possible jet cocoon, linked to the slow wind (Sec. 6.4) is a potential reservoir for a large scale inflow, and we find evidence of an asymmetric inflow towards the nucleus. In addition, the jet launch region must be warped in comparison to the region from where the narrow wind is launched, and nuclear warps are associated with inflows of different angular momentum (Ogilvie & Latter 2013, e.g.). The different orientation and misalignment of the jet with respect to the narrow wind appears to imply a different origin of the jet and wind. However, they may both stem from the same MHD process where a nuclear warp results in different orientations of the outflows.

Rotation of the jet/outflow is an expected feature of MHD jets and winds. If a jet is emerging from the centre of a fast rotating disk, the outflow material is ejected with a significant amount of angular momentum, which may become conserved along the jet streamlines. (Note, there are also other processes that can result in jet rotation (e.g. Fendt 2011; Soker 2005)). Observational evidence for outflow rotation can be found in protostellar jets and winds (e.g. Matthews et al. 2010; Bjerkeli et al. 2016; Hirota et al. 2017; Lee et al. 2017) and in winds and radio jets in AGNs (e.g. Mangham et al. 2017; Raiteri et al. 2017; Britzen et al. 2017) - as well as in the narrow wind in NGC 1377. The velocity in the jet is dominated by rotation right above the disk, until the Alfvén surface (its location is model dependent but for some scenarios $Z_A \simeq 10 \times r_0$ (Cabrit et al. 1999)). Well above the Alfvén surface (Z_A=1-3 pc) the jet velocity should be mostly vertical and v_{out} is likely the maximum allowed velocity of $\sim$600 km s^{-1}. The jet rotation signature should be significantly lower than the jet velocity and may also be difficult to spatially resolve. Therefore, we adopt an estimate to the jet rotation of $\sim$60 km s^{-1} from the estimates of jet dispersion.

The launch region of an MHD jet can be estimated using the formalism of Anderson et al. (2003). They argue that astrophysical magnetocentrifugal jets should be capable of escaping the potential well of the central object fairly easily. Hence the kinetic energy of the jet is higher than the gravitational binding energy at the launch point. Inserting an outflow velocity of $v_{out}\sim$600 km s^{-1}, jet radius $r_{jet}\sim$3 pc, a far-field jet rotational component of 60 km s^{-1}, and the mass of the central object of 9×10^6 M$_\odot$, into their equation (5) yields a launch radius for the molecular jet of $r_{launch}\sim$0.4 pc. This is inside the nuclear dust concentration, but still more than an order of magnitude larger than the dust sublimation radius (Aalto et al. 2017).

The precession time-scale of the molecular jet of NGC 1377 is relatively long, 0.42 Myr for a jet velocity of 600 km s^{-1} for it to be associated with the orbital time for the jet launch region implying. Aalto et al. (2016) discuss possible origins of the precession (see their Sec. 4.1.4) including a misalignment between the spin orientation of the black hole and the accretion disk, an uneven accretion flow or driving by a binary SMBH. Further studies are required to link the cause of the direction changes of the jet to the jet launching mechanism.

In some aspects, the MHD molecular jet suggested here is similar to those found in the early stages of protostellar growth. The similarity lies in the morphology and structure of the molecular jet, as well as harbouring a compact, embedded object. However, the nature of the central object and the time-scales involved are very different. This is expected to impact the relative properties of a protostellar and NGC 1377-like outflow in significant ways.

7.4. Alternative jet-driving mechanisms

The possibility of a faded or under-luminous, quenched jet entraining the gas in NGC 1377 is discussed by Aalto et al. (2016). It is possible that the SMBH of NGC 1377 is growing due to an advection dominated accretion flow (ADAF) (e.g. Abramowicz et al. 1988; Heckman & Best 2014), which would allow for high accretion rates accompanied with low radiation. ADAF flows are, however, expected to result in powerful relativistic radio jets (e.g. Sądowski et al. 2013) and the extreme radio-quietness of NGC 1377 is a challenge to such a model. Alternatively, entrainment and acceleration may be carried out by a hot, thermal jet with a radius that is significantly smaller than that of the molecular jet, and unresolvable by our current ALMA beam. It is not clear if such a jet could harbour the necessary kinetic energy to carry out the molecular gas.

8. The nature of the large-scale molecular disk

We find a $r\sim$60 pc molecular structure aligned with the stellar disk. However, the molecular rotation velocity is very slow, $v_{rot}\sim$27 km s^{-1}, much too slow for the enclosed stellar mass ($\sim 10^8$ M$_\odot$ inside r=60 pc (estimated from HST H-band image, HST program GO14728, J Gallagher PI)) which would require a gas disk rotation velocity of v_{rot}=75 km s^{-1}. A low inclination, $\sim$20°, would be required for the observed velocity to be consistent with the required v_{rot}. However, there is no indication of a near face-on stellar disk and according to the Hyperleda database, the inclination of NGC 1377 is $\sim$90°. The turbulent line widths (σ=30-50 km s^{-1}) in the disk are higher than the rotational velocity which suggests a thick disk that supports itself by turbulence. This could also explain why no star formation has been detected in the central region of NGC 1377. The turbulence may be for example powered by returning gas from the wind or jet, or from a failed wind. Alternatively, the molecular gas is not

distributed in a disk, but is e.g. a filamentary structure possibly infalling onto the central region of NGC 1377.

9. Potential link between feedback and growth in NGC 1377

The wind and jet of NGC 1377 may constitute a different type of outflow than what is usually found towards AGNs (or starbursts). There is, as of yet, no evidence of a significant hot wind or a radio jet in NGC 1377. Instead the gas may be driven out by a molecular, magneto-centrifugal rotating wind and jet. In this scenario, the outflows are not a direct result of the radiative or mechanical feedback of an AGN, but instead arise as an effect of inflowing gas and a magnetic field. These winds and jets help accretion through removing angular momentum. The estimated obscuration is relatively high ($N(H_2)\simeq 1.8\times10^{24}$cm^{-2}) on scales r= 1.5 pc and the suggested presence of an inflow is consistent with a nucleus still in unstable growth. If the narrow wind+jet molecular mass of $\sim 1\times10^7$ M$_\odot$ recently resided in the inner $r\sim$3 pc the obscuration would have been up to two orders of magnitude higher - rivaling the extreme obscuration of the Compact Obscured Nuclei (CONs) (Costagliola et al. 2013; Sakamoto et al. 2013; Aalto et al. 2015a, 2019). It is possible that NGC 1377 is caught in a post-CON evolutionary phase, where a recent growth spurt with associated wind-outflow activity has removed a significant fraction of obscuring material. However, it is also possible that the suggested link between inflow and outflow in NGC 1377 prevents CON-like obscuring layers to form.

The estimated SMBH mass, $9^{+2}_{-3}\times10^6$ M$_\odot$ inside r=1.4 pc, indicates that it is massive with respect to the stellar velocity dispersion. NGC 1377 is on the upper bound of the $M-\sigma$ relation (e.g. Graham et al. 2011; Greene et al. 2016) that links stellar velocity dispersion to black hole mass. This indicates that a process has grown the SMBH ahead of the stellar component of NGC 1377.

The jet and wind of NGC 1377 are also different through being roughly perpendicular to the stellar disk and not at an oblique angle, unlike known radio-jet driven outflows in, for example, NGC 1068, IC5063, ESO 420-G13 or NGC613 (e.g. García-Burillo et al. 2014; Dasyra et al. 2015; Audibert et al. 2019; Fernández-Ontiveros et al. 2020). The molecular jet of NGC 1377 may have more in common with the collimated molecular outflows recently discovered towards galaxies with CONsi (e.g. Falstad et al. 2018; Barcos-Muñoz et al. 2018; Falstad et al. 2019). The jet and narrow wind are surrounded by a slow wind of gas which may partially be stemming from internal and external shocks in the jet producing a cocoon or an envelope of gas (Sec. 6.4). This material has low angular momentum and low-velocity which means that it is readily available to fuel nuclear growth.

We find tentative evidence of inflowing gas (on several scales) that could help power the disk-wind and fuel the nuclear growth. Further observations and modelling are required to determine the inflow rate and the origin of the inflowing gas. It is possible that it is coming from the enveloping cocoon with an origin in the wind and jet gas. if so, the SMBH of NGC 1377 has a substantial supply of gas that, eventually if star formation is prevented, can serve as fuel for SMBH growth. Such a feeding-cycle could also provide part of the answer to the question of the origin of the molecular gas concentration (Aalto et al. 2012). In this ageing, post-starburst galaxy, a circulation system may explain why there is still a significant reservoir of molecular gas.

The nuclear luminosity implies a relatively high current accretion state of NGC 1377, but it is not enough to significantly grow the SMBH. With the estimated, radiative, accretion rate, the SMBH would grow with only $10^{-3}-10^{-2}$ M$_\odot$ per year and, it would take at least 100 Myr for the SMBH to double its mass. However, it is likely that the nuclear luminosity and accretion rate was significantly higher in the recent past, giving rise to the molecular jet and wind. Alternatively, NGC 1377 is, or recently has been, in a state of advective dominated accretion where the energy is not radiated.

10. Conclusions

With high-resolution (0.″02×0.″03 (2×3 pc)) ALMA 345 GHz observations of CO 3–2, HCO$^+$ 4–3, vibrationally excited HCN 4–3 v_2=1f, and continuum we have studied the remarkable, radio-quiet, and collimated molecular jet and wind of the lenticular galaxy NGC 1377.

The morphology and structure of the jet and wind is resolved, revealing clumpy, turbulent emission with high gas dispersion (σ>40 km s^{-1}) and a radial excitation gradient in the gas. The jet is narrow with an average width of 3-7 pc, but it undergoes an apparent expansion 20-40 pc from the nucleus where the jet broadens to 10-17 pc. This widening of the jet may be caused by bow shocks from jet-wind interactions or internal working surfaces stemming from variations in the outflow speed. The molecular jet has a length of 150 pc and appears to be launched from $r\lesssim$0.4 pc. It shows velocity reversals that we propose are either due to regular precession or more episodic directional changes of ejection. We estimate the precession angle to 15° and the jet outflow speed to ~600 km s^{-1}.

The jet has a high momentum flux $\dot{M}v=\dot{p}$ of $\sim 37L/c$ which is in general consistent both with AGN feedback and momentum fluxes found for early stage protostellar feedback. However, the luminosity of the nuclear source may have varied considerably during the duration of the outflow, rendering the value of $\dot{p}$ uncertain. We propose that the molecular jet is a gravitationally powered magneto-centrifugal wind, but cannot exclude entrainment by a hitherto undetected, weak radio or thermal jet. There is enough kinetic energy in the jet to power the high levels of turbulence in the wind and disk. Jet-wind interactions in the form of bow-shocks are possible processes of transfer.

The jet is surrounded by a narrow molecular wind of opening angle 50° - 70°, which is is launched from the inner (r=1.5-3 pc) region of NGC 1377. We find strong evidence of wind-rotation and suggest that also the narrow wind is a magneto-centrifugal wind, and that it appears to be primarily direct driven. Its outflow velocities are 90±30 km s^{-1} with a significant momentum flux of $\dot{p}=7L/c$. Radiation pressure cannot be excluded as an auxiliary driving force, but the relatively narrow opening angle is consistent with a magnetically confined wind. The narrow wind and jet are misaligned which is expected from the signatures of nuclear warping and the misalignment can result in jet-wind interactions.

The jet and narrow wind are enveloped by a slow wind which we propose is a cocoon, forming from the jet-wind interaction or from gas ejected in internal working surfaces of the jet.

An r=2 pc, asymmetric, torus-like dust structure is found in 0.8 mm continuum. It also shows compact emission from vibrationally excited HCN. The nuclear dust emission is hot with inferred T_d>180 K and is near Compton Thick with an estimated gas column density of $N(H_2)\simeq 1.8\times10^{24}$cm^{-2}. We estimate the luminosity of the nuclear dust source to $\sim 4.8\times10^9$ L$_\odot$. Absence of signs of ongoing star formation lead us to suggest that it stems from accretion onto the dust-enshrouded SMBH. The nuclear high-velocity gas is consistent with dynamical mass of $9^{+2}_{-3}\times10^6$ M$_\odot$ inside r=1.4 pc. The lopsided, obscuring torus appears to be

a dynamically active region, harbouring both in- and outflows. High-velocity blue-shifted gas (in CO and $H^{13}CN$) located 2 pc west of the nucleus may be a signature of gas on highly non-circular orbits, but the presence of a second nucleus can not yet be dismissed. Larger scale (r=60 pc) emission aligned with the stellar disk is rotating too slowly for its enclosed mass and may be a pressure-supported, turbulent disk (or is not actually a molecular disk.)

We suggest that the SMBH of NGC 1377 is in a state of moderate growth, at the end of a more intense phase of activity and possibly also from a state of more extreme nuclear obscuration. The SMBH of NGC 1377 appears massive with respect to its stellar velocity dispersion and this opens new questions on SMBH growth processes in obscured, dusty galaxies. The nuclear growth may be fueled by low-angular momentum gas inflowing from the gas ejected in the molecular jet and wind. In this scenario, the molecular jet, wind and potential inflow represent a feedback loop of cyclic, central accretion which may be an important phase in the evolution of NGC 1377. In this ageing, post-starburst galaxy, such a circulation system may explain why there is still a significant reservoir of molecular gas. Further studies are required to investigate if an over-massive SMBH is an expected consequence of an outflow-powered feedback loop.

Acknowledgements. This paper makes use of the following ALMA data: ADS/JAO.ALMA#2012.1.00900.S. ALMA is a partnership of ESO (representing its Member States), NSF (USA), and NINS (Japan), together with NRC (Canada) and NSC and ASIAA (Taiwan), in cooperation with the Republic of Chile. The Joint ALMA Observatory is operated by ESO, AUI/NRAO, and NAOJ. We thank the Nordic ALMA ARC node for excellent support. S.A. gratefully acknowledges support from an ERC Advanced Grant 789410 and from the Swedish Research Council. K.S. was supported by grant MOST 102-2119-M-001-011-MY3 S.G.B. acknowledges the economic support from grants ESP2015-68964-P and AYA2016-76682-C3-2-P. This research has made use of the NASA/IPAC Extragalactic Database (NED) which is operated by the Jet Propulsion Laboratory, California Institute of Technology, under contract with the National Aeronautics and Space Administration.

References

Aalto, S., Costagliola, F., Muller, S., et al. 2016, A&A, 590, A73
Aalto, S., Costagliola, S. M. F., Gonzalez-Alfonso, E., et al. 2015a, ArXiv e-prints [arXiv:1504.06824]
Aalto, S., Garcia-Burillo, S., Muller, S., et al. 2015b, A&A, 574, A85
Aalto, S., Garcia-Burillo, S., Muller, S., et al. 2015c, A&A, 574, A85
Aalto, S., Muller, S., Costagliola, F., et al. 2017, A&A, 608, A22
Aalto, S., Muller, S., König, S., et al. 2019, A&A, 627, A147
Aalto, S., Muller, S., Sakamoto, K., et al. 2012, A&A, 546, A68
Abramowicz, M. A., Czerny, B., Lasota, J. P., & Szuszkiewicz, E. 1988, ApJ, 332, 646
Anderson, J. M., Li, Z.-Y., Krasnopolsky, R., & Blandford, R. D. 2003, ApJ, 590, L107
Audibert, A., Combes, F., García-Burillo, S., et al. 2019, A&A, 632, A33
Barcos-Muñoz, L., Aalto, S., Thompson, T. A., et al. 2018, ApJ, 853, L28
Bjerkeli, P., van der Wiel, M. H. D., Harsono, D., Ramsey, J. P., & Jørgensen, J. K. 2016, Nature, 540, 406
Blandford, R. D. 1998, in American Institute of Physics Conference Series, Vol. 431, American Institute of Physics Conference Series, ed. S. S. Holt & T. R. Kallman, 43–52
Blandford, R. D. & Payne, D. G. 1982, MNRAS, 199, 883
Bontemps, S., Andre, P., Terebey, S., & Cabrit, S. 1996, A&A, 311, 858
Britzen, S., Qian, S. J., Steffen, W., et al. 2017, A&A, 602, A29
Cabrit, S., Ferreira, J., & Raga, A. C. 1999, A&A, 343, L61
Cao, X. 2012, MNRAS, 426, 2813
Caselli, P., Walmsley, C. M., Zucconi, A., et al. 2002, ApJ, 565, 344
Cicone, C., Maiolino, R., Sturm, E., et al. 2014, A&A, 562, A21
Combes, F., García-Burillo, S., Audibert, A., et al. 2019, A&A, 623, A79
Costagliola, F., Aalto, S., Sakamoto, K., et al. 2013, A&A, 556, A66
Costagliola, F., Herrero-Illana, R., Lohfink, A., et al. 2016, A&A, 594, A114
Dasyra, K. M., Bostrom, A. C., Combes, F., & Vlahakis, N. 2015, ArXiv e-prints [arXiv:1503.05484]
Evans, Neal J., I. 1999, ARA&A, 37, 311
Falstad, N., Aalto, S., Mangum, J. G., et al. 2018, A&A, 609, A75
Falstad, N., Hallqvist, F., Aalto, S., et al. 2019, A&A, 623, A29
Fendt, C. 2011, ApJ, 737, 43
Fernández-Ontiveros, J. A., Dasyra, K. M., Hatziminaoglou, E., et al. 2020, A&A, 633, A127
Ferreira, J., Dougados, C., & Cabrit, S. 2006, A&A, 453, 785
Ferreira, J. & Petrucci, P. O. 2011, in IAU Symposium, Vol. 275, Jets at All Scales, ed. G. E. Romero, R. A. Sunyaev, & T. Belloni, 260–264
Feruglio, C., Maiolino, R., Piconcelli, E., et al. 2010, A&A, 518, L155+
Fiore, F., Feruglio, C., Shankar, F., et al. 2017, A&A, 601, A143
Fluetsch, A., Maiolino, R., Carniani, S., et al. 2019, MNRAS, 483, 4586
Gallimore, J. F., Elitzur, M., Maiolino, R., et al. 2016, ApJ, 829, L7
García-Burillo, S., Combes, F., Ramos Almeida, C., et al. 2019, A&A, 632, A61
García-Burillo, S., Combes, F., Ramos Almeida, C., et al. 2016, ApJ, 823, L12
García-Burillo, S., Combes, F., Usero, A., et al. 2014, A&A, 567, A125
Graham, A. W., Onken, C. A., Athanassoula, E., & Combes, F. 2011, MNRAS, 412, 2211
Greene, J. E., Seth, A., Kim, M., et al. 2016, ApJ, 826, L32
Heckman, T. M. & Best, P. N. 2014, ARA&A, 52, 589
Helou, G., Soifer, B. T., & Rowan-Robinson, M. 1985, ApJ, 298, L7
Hirota, T., Machida, M. N., Matsushita, Y., et al. 2017, Nature Astronomy, 1, 0146
Ho, L. C. 2004, in 35th COSPAR Scientific Assembly, Vol. 35, 921
Hone, E., Kraus, S., Kreplin, A., et al. 2017, A&A, 607, A17
Hopkins, P. F., Hayward, C. C., Narayanan, D., & Hernquist, L. 2012, MNRAS, 420, 320
Imanishi, M. 2006, AJ, 131, 2406
Imanishi, M., Imase, K., Oi, N., & Ichikawa, K. 2011, AJ, 141, 156
Imanishi, M., Nakanishi, K., Tamura, Y., & Peng, C. 2009, AJ, 137, 3581
Impellizzeri, C. M. V., Gallimore, J. F., Baum, S. A., et al. 2019, ApJ, 884, L28
Izumi, T., Wada, K., Fukushige, R., Hamamura, S., & Kohno, K. 2018, ApJ, 867, 48
Keene, J., Hildebrand, R. H., & Whitcomb, S. E. 1982, ApJ, 252, L11
Kocevski, D. D., Brightman, M., Nandra, K., et al. 2015, ApJ, 814, 104
Lee, C.-F., Ho, P. T. P., Li, Z.-Y., et al. 2017, Nature Astronomy, 1, 0152
Lusso, E., Hennawi, J. F., Comastri, A., et al. 2013, ApJ, 777, 86
Maiolino, R., Russell, H. R., Fabian, A. C., et al. 2017, Nature, 544, 202
Mangham, S. W., Knigge, C., Matthews, J. H., et al. 2017, MNRAS, 471, 4788
Matsushita, S., Muller, S., & Lim, J. 2007, A&A, 468, L49
Matthews, L. D., Greenhill, L. J., Goddi, C., et al. 2010, ApJ, 708, 80
McBride, J., Robishaw, T., Heiles, C., Bower, G. C., & Sarma, A. P. 2015, MNRAS, 447, 1103
Morganti, R., Oosterloo, T., Oonk, J. B. R., Frieswijk, W., & Tadhunter, C. 2015, A&A, 580, A1
Ogilvie, G. I. & Latter, H. N. 2013, MNRAS, 433, 2403
Ohyama, Y., Sakamoto, K., Aalto, S., & Gallagher, John S., I. 2019, ApJ, 871, 191
Ostriker, E. C. 1997, ApJ, 486, 291
Ouyed, R. & Pudritz, R. E. 1997, ApJ, 484, 794
Oya, Y., Sakai, N., Sakai, T., et al. 2014, ApJ, 795, 152
Panoglou, D., Cabrit, S., Pineau Des Forêts, G., et al. 2012, A&A, 538, A2
Pereira-Santaella, M., Colina, L., García-Burillo, S., et al. 2018, A&A, 616, A171
Pudritz, R. E. & Banerjee, R. 2005, in IAU Symposium, Vol. 227, Massive Star Birth: A Crossroads of Astrophysics, ed. R. Cesaroni, M. Felli, E. Churchwell, & M. Walmsley, 163–173
Raga, A., Cabrit, S., Dougados, C., & Lavalley, C. 2001, A&A, 367, 959
Raiteri, C. M., Villata, M., Acosta-Pulido, J. A., et al. 2017, Nature, 552, 374
Ricci, C., Trakhtenbrot, B., Koss, M. J., et al. 2017, Nature, 549, 488
Roussel, H., Helou, G., Beck, R., et al. 2003, ApJ, 593, 733
Roussel, H., Helou, G., Smith, J. D., et al. 2006, ApJ, 646, 841
Sakamoto, K., Aalto, S., Costagliola, F., et al. 2013, ApJ, 764, 42
Sakamoto, K., Aalto, S., Evans, A. S., Wiedner, M. C., & Wilner, D. J. 2010, ApJ, 725, L228
Shu, F. H., Najita, J., Ostriker, E. C., & Shang, H. 1995, ApJ, 455, L155
Sądowski, A., Narayan, R., Penna, R., & Zhu, Y. 2013, MNRAS, 436, 3856
Soker, N. 2005, A&A, 435, 125
Spoon, H. W. W., Marshall, J. A., Houck, J. R., et al. 2007, ApJ, 654, L49
Tabone, B., Raga, A., Cabrit, S., & Pineau des Forêts, G. 2018, A&A, 614, A119
Tafalla, M., Su, Y. N., Shang, H., et al. 2017, A&A, 597, A119
Todo, Y., Uchida, Y., Sato, T., & Rosner, R. 1993, ApJ, 403, 164
Tristram, K. R. W., Burtscher, L., Jaffe, W., et al. 2014, A&A, 563, A82
Veilleux, S., Trippe, M., Hamann, F., et al. 2013, ApJ, 764, 15
Vollmer, B., Schartmann, M., Burtscher, L., et al. 2018, A&A, 615, A164
Wada, K. 2012, ApJ, 758, 66
Yoast-Hull, T. M. & Murray, N. 2019, MNRAS, 484, 3665

[1] Department of Space, Earth and Environment, Onsala Space Observatory, Chalmers University of Technology, SE-439 92 Onsala, Sweden
e-mail: saalto@chalmers.se
[2] Kagoshima University, Kagoshima 890-0065, Japan
[3] Department of Astronomy, University of Wisconsin-Madison, 5534 Sterling, 475 North Charter Street, Madison WI 53706, USA
[4] Institute of Astronomy and Astrophysics, Academia Sinica, PO Box 23-141, 10617 Taipei, Taiwan
[5] Department of Astrophysics, Astronomy & Mechanics, Faculty of Physics, University of Athens, Panepistimiopolis Zografos 15784, Greece
[6] Observatoire de Paris, LERMA (CNRS:UMR8112), 61 Av. de l'Observatoire, 75014 Paris, France
[7] Observatorio Astronómico Nacional (OAN)-Observatorio de Madrid, Alfonso XII 3, 28014-Madrid, Spain
[8] European Southern Observatory, Alonso de Córdova 3107, Vitacura, Santiago, Chile
[9] Joint ALMA Observatory, Alonso de Córdova 3107, Vitacura, Santiago, Chile
[10] University of Tokyo
[11] Leiden Observatory, Leiden University, 2300 RA, Leiden, The Netherlands
[12] University of Virginia, Charlottesville, VA 22904, USA, NRAO, 520 Edgemont Road, Charlottesville, VA 22903, USA
[13] Finnish Centre for Astronomy with ESO (FINCA), University of Turku, Väisäläntie 20, FI-21500 Kaarina, Finland